



**HAL**  
open science

## Soil moisture retrieval over irrigated grassland using X-band SAR data

Mohammad El Hajj, N. Baghdadi, Mehrez Zribi, Gilles Belaud, B. Cheviron,  
Dominique Courault, F. Charron

► **To cite this version:**

Mohammad El Hajj, N. Baghdadi, Mehrez Zribi, Gilles Belaud, B. Cheviron, et al.. Soil moisture retrieval over irrigated grassland using X-band SAR data. *Remote Sensing of Environment*, 2016, 176, pp.202-218. 10.1016/j.rse.2016.01.027. hal-01336862

**HAL Id: hal-01336862**

**<https://hal.science/hal-01336862>**

Submitted on 24 Jun 2016

**HAL** is a multi-disciplinary open access archive for the deposit and dissemination of scientific research documents, whether they are published or not. The documents may come from teaching and research institutions in France or abroad, or from public or private research centers.

L'archive ouverte pluridisciplinaire **HAL**, est destinée au dépôt et à la diffusion de documents scientifiques de niveau recherche, publiés ou non, émanant des établissements d'enseignement et de recherche français ou étrangers, des laboratoires publics ou privés.



Distributed under a Creative Commons Attribution - NonCommercial - NoDerivatives 4.0  
International License

1 El Hajj M., Baghdadi N., Zribi M., Belaud G., Cheviron B., Courault D., and  
2 Charron F., 2016. Soil moisture retrieval over irrigated grassland using X-  
3 band SAR data. *Remote Sensing of Environment*, vol. 176, pp. 202-218, doi:  
4 <http://dx.doi.org/10.1016/j.rse.2016.01.027>.  
5

## 6

# 7 Soil moisture retrieval over irrigated grassland using 8 X-band SAR data

9

10 **Mohammad El Hajj <sup>1,\*</sup>, Nicolas Baghdadi <sup>1</sup>, Mehrez Zribi <sup>2</sup>, Gilles Belaud <sup>3</sup>, Bruno  
11 Cheviron <sup>4</sup>, Dominique Courault <sup>5</sup>, François Charron <sup>3</sup>**

12

13 <sup>1</sup> IRSTEA, UMR TETIS, 500 rue François Breton, 34093 Montpellier cedex 5, France

14 <sup>2</sup> CNRS, CESBIO, 18 av. Edouard Belin, bpi 2801, 31401 Toulouse cedex 9, France

15 <sup>3</sup> SupAgro, UMR G-EAU, 2 place Pierre Viala, 34060 Montpellier, France

16 <sup>4</sup> IRSTEA, UMR G-EAU, 361 rue François Breton, 34196 Montpellier cedex 5, France

17 <sup>5</sup> INRA, UMR 1114 EMMAH, Domaine St. Paul, 84914, Avignon, France  
18

---

19 **Abstract:** The aim of this study was to develop an inversion approach to estimate surface soil  
20 moisture from X-band SAR data over irrigated grassland areas. This approach simulates a  
21 coupling scenario between Synthetic Aperture Radar (SAR) and optical images through the  
22 Water Cloud Model (WCM). A time series of SAR (TerraSAR-X and COSMO-SkyMed) and

23 optical (SPOT 4/5 and LANDSAT 7/8) images were acquired over an irrigated grassland region  
24 in southeastern France.

25 An inversion technique based on multi-layer perceptron neural networks (NNs) was used to  
26 invert the Water Cloud Model (WCM) for soil moisture estimation. Three inversion  
27 configurations based on SAR and optical images were defined: (1) HH polarization, (2) HV  
28 polarization, and (3) both HH and HV polarizations, all with one vegetation descriptor derived  
29 from optical data. The investigated vegetation descriptors were the Normalized Difference  
30 Vegetation Index "NDVI", Leaf Area Index "LAI", Fraction of Absorbed Photosynthetically  
31 Active Radiation "FAPAR", and the Fractional vegetation COVER "FCOVER". These  
32 vegetation descriptors were derived from optical images. For the three inversion configurations,  
33 the NNs were trained and validated using a noisy synthetic dataset generated by the WCM for a  
34 wide range of soil moisture and vegetation descriptor values. The trained NNs were then  
35 validated from a real dataset composed of X-band SAR backscattering coefficients and  
36 vegetation descriptor derived from optical images. The use of X-band SAR measurements in HH  
37 polarization (in addition to one vegetation descriptor derived from optical images) yields more  
38 precise results on soil moisture ( $M_v$ ) estimates. In the case of NDVI derived from optical images  
39 as the vegetation descriptor, the Root Mean Square Error on  $M_v$  estimates was 3.6 Vol.% for  
40 NDVI values between 0.45 and 0.75, and 6.1 Vol.% for NDVI between 0.75 and 0.90. Similar  
41 results were obtained regardless of the other vegetation descriptor used.

42 **Keywords:** grassland; TerraSAR-X; COSMO-SkyMED; neural networks; inversion; soil  
43 moisture; vegetation indices

## 44 **1. Introduction**

45 Monitoring the spatio-temporal evolution of soil moisture over irrigated grassland areas is of  
46 crucial importance for effective irrigation and crop management (Allen et al., 1998; Brereton and  
47 Hope-Cawdery, 1988; Hong et al., 2013; Leenhardt et al., 2004; Merot et al., 2008). In situ  
48 sensors to measure soil moisture are costly and provide only local information. Thus, these  
49 sensors are not sufficient for monitoring the soil moisture in huge irrigated grassland areas  
50 because the soil moisture presents large heterogeneities due to environmental characteristics and  
51 irrigation practices. SAR (Synthetic Aperture Radar) data have shown great potential to provide  
52 spatially distributed surface soil moisture measurements over bare and vegetated soil (Aubert et  
53 al., 2011; Baghdadi et al., 2012a; Gherboudj et al., 2011; Paloscia et al., 2008, 2013; Prevot et  
54 al., 1993; Santi et al., 2013). Due to their ability to operate in all weather conditions, SAR  
55 sensors offer the opportunity to monitor and quantify the surface soil moisture at a large scale  
56 with high spatial and temporal resolution.

57 SAR remote sensing was widely and primarily used to estimate the soil moisture and surface  
58 roughness. Over bare soil (or soil with little vegetation cover) the estimation of soil moisture was  
59 performed using either a physical (e.g the Integral Equation Model, Fung et al., 1992) or  
60 statistical (e.g Dubois and Oh models, Dubois et al., 1995; Oh, 2004) model in an inversion  
61 scheme. In contrast to physical models, statistical models need to be calibrated using in situ  
62 measurement and SAR observation acquired over the study area. Moreover, the use of statistical  
63 models is limited to the ranges of data variation used for calibration. Most of the studies used  
64 radar data in the X- and C-bands to estimate the soil moisture of bare soil and have shown good  
65 results, with an accuracy between 3 and 6 Vol.% (Aubert et al., 2011; Baghdadi et al., 2012a;  
66 Srivastava et al., 2003, 2009; Zribi et al., 2005).

67 The presence of vegetation cover complicates soil moisture retrieval from SAR data because  
68 vegetation canopy not only introduces two-way attenuation in SAR backscatter from soil, but  
69 also contributes its own backscatter (He et al., 2014; Srivastava et al., 2011). Most studies used  
70 the Water Cloud Model (WCM) in an inversion scheme for soil moisture estimation over areas  
71 with vegetated cover. In the WCM the total reflected radar signal is modeled as a function of the  
72 vegetation and soil contribution. The vegetation contribution, direct scattering and attenuation, is  
73 computed mainly using one biophysical parameter representing the vegetation effect. This  
74 biophysical parameter could be estimated from optical data. Therefore, it is important to combine  
75 SAR and optical data for operational mapping of soil moisture over areas covered by vegetation  
76 (Fieuzal et al., 2011; He et al., 2014; Hosseini and Saradjian, 2011; Notarnicola et al., 2006;  
77 Prakash et al., 2012). Currently, the high temporal repetitiveness of X-band (at least one day in  
78 case of TSX and CSK) and optical (between 16 and 26 days for Landsat-7/8 and SPOT-4/5 data,  
79 respectively) data makes the combined use of SAR and optical data for soil and vegetation  
80 parameter monitoring more reliable in near real time.

81 Optical data have shown a great potential to estimate biophysical parameters of vegetation.  
82 These parameters can be derived from optical data using physical and statistical models. Physical  
83 models (e.g PROSAIL, and SAFY) invert the vegetation spectral reflectance and estimate the  
84 biophysical parameters of the vegetation (Botha et al., 2010; Ceccato et al., 2001; Darvishzadeh  
85 et al., 2008; Fieuzal et al., 2011). Most statistical models are based on direct relationships  
86 between the Normalized Differential Vegetation Index (NDVI) and the measured biophysical  
87 parameters of vegetation, such as the LAI of wheat, grasslands, maize, corn and rice (Baret and  
88 Guerif, 2006; Baret et al., 2007; Bsaibes et al., 2009; Courault et al., 2008, 2010)

89 The possibility of retrieving soil parameters from vegetated surfaces was widely investigated  
90 using C-band configurations, whereas few studies were carried out using X-band data. Hajj *et al.*  
91 (2014) showed that the radar signal penetration depth in the X-band (incidence about 30°) is  
92 high, even in dense grass cover (HVE "Vegetation Height" about 1m, BIO "Biomass" up to 3.9  
93 kg/m<sup>2</sup>). These results encourage the use of X-band with medium angle (about 30°) in both HH  
94 and HV polarizations for soil moisture estimates over grassland. For C and X-bands SAR data,  
95 studies showed that it is possible to estimate the soil moisture with accuracy from 2 to 8 Vol.%  
96 (RMSE "Root Mean Square Error") (Gherboudj *et al.*, 2011; He *et al.*, 2014; Notarnicola *et al.*,  
97 2006; Prévot *et al.*, 1993; Sikdar and Cumming, 2004; Wang *et al.*, 2011; Yang *et al.*, 2012; Yu  
98 and Zhao, 2011; Zribi *et al.*, 2011).

99 The aim of this study is to evaluate the potential of X-band SAR data combined with optical  
100 data to estimate soil moisture over irrigated grassland areas located in southeastern France. An  
101 approach based on the inversion of the WCM using multi-layer neural networks (NNs) was  
102 developed. This approach relies on four main steps: (1) parameterize the WCM, (2) simulate  
103 learning the SAR synthetic dataset, (3) train the neural networks according to three inversion  
104 configurations using a part of the synthetic dataset, and finally (4) apply the trained NNs on  
105 synthetic and real datasets to validate the inversion approach. In this paper, section 2 presents the  
106 study areas and the ground-truth measurements performed in situ. Section 3 describes the  
107 methodology. The results are shown in section 4. Finally, section 5 presents the principal  
108 conclusions.

## 109 **2. Study area and in situ measurements**

### 110 2.1 Study area

111 The study area, named "Domaine de Merle", is an experimental farm located in southeastern  
112 France (centered at 43.64° N, 5.00° E). Its extent is approximately 400 hectares, among which  
113 150 hectares are irrigated grassland for hay production (Figure 1). The produced hay is high-  
114 value with a Certified Origin Product label (COP) thanks to the specific environmental  
115 conditions and conventional irrigation guidelines.

116 The climate is Mediterranean with a rainy season between September and November. The  
117 average cumulative rainfall collected at the study site reached 457.5 mm in 2013, and in general  
118 varies between 350 mm and 800 mm over the past 20 years (Courault et al., 2010). The mean air  
119 temperature is approximately 8°C and 24°C during winter and summer, respectively (Courault et  
120 al., 2010). The in situ measured evaporation rate (potential evapotranspiration) can reach 10  
121 mm/day during the summer due to high temperatures associated with dry and windy conditions.  
122 Meteorological instruments installed in the study area allow for recording hourly temperature  
123 and precipitation.

124 The topsoil texture of irrigated plots is stony loam (15% to 20% pebbles) with the depth  
125 varying from 30 cm to 80 cm, depending on the plot age (between 10 years and 3 centuries)  
126 (Bottraud et al., 1984; Mérot, 2007). The soil is always very smooth thanks to regular irrigation  
127 (approximately every 10 days) by gravity. Moreover, the soil has a moderate retention capacity,  
128 with concentrated vegetation roots in the upper 30 cm (Merot et al., 2008).

129 Plots were leveled with a very gentle slope to allow irrigation by gravity (border irrigation).  
130 Irrigation is applied by means of canals which bring water to the highest extremities of the plots.

131 Each plot is irrigated every 10 days on average from April to September. Plots are harvested  
132 three times a year, in May, July, and September.



133

134 **Figure 1.** Location of the study site (Domaine du Merle). Black polygons delineate training  
135 irrigated grassland plots where ground measurements were made.

## 136 2.2 SAR Images

137 Twenty three X-band SAR images were acquired by the COSMO-SkyMed (CSK) and  
138 TerraSAR-X (TSX) sensors between April and October 2013. All SAR images are in dual-  
139 polarization mode (HH and HV) with incidence angles between  $28.3^\circ$  and  $32.5^\circ$  (Table 1).  
140 Moreover, TSX and CSK images are in Stripmap (pixel spacing of 3 m) and Stripmap Pingpong  
141 (pixel spacing of 8 m) imaging modes, respectively.

142 Radiometric calibration of SAR images was performed using algorithms developed by the  
143 German Aerospace Center (DLR) and the Italian Space Agency (ASI). The radiometric  
144 calibration transforms the digital number of each pixel ( $DN_i$ ) to a radar backscattering coefficient

145 ( $\sigma_i^\circ$ ). For the seven TSX MGD (Multi Look Ground Range Detected), the radiometric  
146 calibrations were performed according to the following equation (Eineder et al., 2008):

$$\sigma_i^\circ = K_s \cdot DN_i^2 \cdot \sin(\theta) - NESZ \quad (\text{Eq. 1})$$

147 where  $K_s$  is the calibration constant,  $\theta$  is the reference incidence angle, and NESZ is the Noise  
148 Equivalent Sigma Zero.

149 For the sixteen CSK images,  $\sigma_i^\circ$  was computed from the  $DN_i$  using the following equation:

$$\sigma_i^\circ = DN_i^2 \cdot \frac{1}{K \cdot F^2} \cdot \sin(\theta) R_{\text{ref}}^{2 \cdot R_{\text{exp}}} \quad (\text{Eq. 2})$$

150  
151 where  $R_{\text{ref}}$  is the reference slant range,  $R_{\text{exp}}$  is the reference slant range exponent,  $K$  is the  
152 calibration constant, and  $F$  is the rescaling factor.

153 Values of parameters given in Equations 1 and 2 are given in the metadata associated with  
154 each TSX and CSK image. The  $\sigma_i^\circ$  were then averaged for each grassland plot and converted to  
155 the decibel scale according to the following equation:

$$\sigma_{\text{dB}}^\circ = 10 \cdot \log_{10}(\sum \sigma_i^\circ) \quad (\text{Eq. 3})$$

156 The number of looks used to generate a pixel spacing of 3 m x 3 m is one look in both the  
157 range and the azimuth. However, to generate a pixel spacing of 8 m x 8 m, the number of looks  
158 is one look in the range and four in the azimuth. The radar image pixel count in the training plots  
159 is between 521 and 1686 pixels for the CSK images, and between 3425 and 11320 for the TSX  
160 images.

161 For training plots, a comparison was performed between the backscattering coefficients (in  
162 both HH and HV polarizations) derived from one TSX and one CSK image, both acquired on the  
163 same day (08/07/2013) with about 40 minutes time interval. For such time interval the soil and  
164 vegetation conditions remain unchanged. For both HH and HV polarizations, results showed  
165 unbiased comparison with low Root Mean Square Error (RMSE ~ 0.4 dB), low Mean Absolute  
166 Percentage Error (MAPE < 5 %) and high correlation coefficient ( $R^2 \sim 0.9$ ).

### 167 2.3 Optical Images

168 Thirty optical images were acquired by SPOT-4, SPOT-5, LANDSAT-7 and LANDSAT-8  
169 between April and October 2013 at dates very close to the SAR images (Table 1). The  
170 calibration of optical images includes correction for atmospheric effects and ortho-rectification.  
171 SPOT-4 images were calibrated by the CESBIO (Centre d'Etudes Spatiales de la BIOSphère) in  
172 the framework of the Take 5 experiment (<http://www.cesbio.ups-tlse.fr/>). Atmospheric correction  
173 of SPOT-4 images was performed according to the method described in the study of Hagolle *et*  
174 *al.* (2008). SPOT-5 and LANDSAT-8 were corrected for atmospheric effects using the  
175 Simplified Method of Atmospheric Correction (SMAC) (Rahman and Dedieu, 1994). The  
176 SMAC model transforms the TOA reflectance (Top Of Atmosphere) to an atmospherically  
177 corrected reflectance. Input data to the SMAC model, the Aerosol Optical Thickness (AOT) at  
178 550 nm, the water vapor content ( $\text{g/m}^2$ ), and Ozone, were obtained from the AERONET  
179 (Aerosol Robotic NETwork) website (<http://aeronet.gsfc.nasa.gov/>). LANDSAT-7 images,  
180 already corrected for atmospheric effects, were downloaded directly from the website of the  
181 USGS (<http://earthexplorer.usgs.gov/>). The atmospheric correction of LANDSAT-7 images  
182 were carried out by NASA (National Aeronautics and Space Administration) by applying the 6S  
183 (Second Simulation of a Satellite Signal in the Solar Spectrum) radiative transfer model data as

184 described by Masek et al. (2013) . Finally, LANDSAT-7/8 images were already ortho-rectified,  
185 whereas SPOT-5 images were ortho-rectified using the terrain correction module implemented in  
186 the ERDAS imaging software. The optical image pixel count in the training plots is between 39  
187 and 108 for LANDSAT images, and between 79 and 223 for SPOT images.

188 The NDVI was computed from the optical images. Then, NDVI pixel values were averaged  
189 for each plot. For all training plots, a comparison was performed between NDVI derived from  
190 images acquired by different sensors (LANDSAT-7/8, SPOT-4/5) with time interval less than  
191 four days. Results showed unbiased comparison with low RMSE ( $\leq 0.04$ ), low MAPE ( $< 5\%$ ),  
192 and good correlation coefficient ( $R^2$  between 0.70 and 0.98). Thus, NDVI derived from different  
193 sensors were comparable.

194

195 **Table 1.** Acquisition dates of SAR and optical images (in 2013). Ground measurements are soil  
 196 moisture and roughness, LAI, FAPAR, FCOVER, BIO, VWC, and HVE (described in section  
 197 below).

	April						May						Jun										July												
	14	17	19	24	25	30	03	04	11	14	22	27	03	04	06	10	11	12	13	14	18	26	28	30	05	08	12	14	16	19	22	29	30		
<b>TSX</b>			X			X				X	X																X						X		
<b>CSK</b>														X	X	X				X		X					X	X		X					
<b>SPOT-4 &amp; 5</b>	X			X				X		X					X			X	X					X	X										
<b>LANDSAT-7 &amp; 8</b>		X		X		X		X			X		X				X						X					X			X		X		
<b>In situ measurement</b>		X			X	X			X	X		X		X	X	X			X	X					X	X		X	X		X	X		X	X

	August											September								October				
	01	09	13	15	20	21	22	23	26	29	31	02	03	04	10	16	22	24	01	04	06	11	16	
<b>TSX</b>																				X				
<b>CSK</b>	X	X							X	X		X			X					X			X	
<b>SPOT-4 &amp; 5</b>	X				X												X				X	X		
<b>LANDSAT-7 &amp; 8</b>				X				X		X						X		X						
<b>In situ measurement</b>	X	X	X	X		X	X		X	X	X	X	X	X					X	X	X		X	

198 2.4 In situ measurements

199 In situ campaigns were conducted simultaneously with SAR acquisitions to collect ground-  
 200 truthed measurements of soil and vegetation parameters in twelve training plots (plots

201 completely flooded or under harvest were not considered). These plots are well levelled and have  
202 enough size to be considered as sampling unit (Patel and Srivastava, 2013). The dimension of  
203 sampled plot ranges between 2.9 ha and 8.80 ha.

#### 204 2.4.1 Soil moisture and roughness

205 Due to the high irrigation frequency and evapotranspiration rates, soil moisture measurements  
206 were performed close in time (within a window of 2 hours) to the satellite overpass. For each  
207 training plot, twenty five to thirty measurements of volumetric soil moisture approximately  
208 evenly distributed in space (on average every 20 m) were conducted in the top 5 cm of soil by  
209 means of a calibrated TDR (Time Domain Reflectometry) probe. Soil moisture was measured in  
210 the top 5 cm of soil because the radar penetration depth is assumed to be a few centimeters in the  
211 X-band (Ulaby et al., 1986). The soil moisture of each plot was represented by the mean of all  
212 soil moisture measurements performed in that plot, except when high spatial variability of soil  
213 moisture was observed. This variability is the result to current or recent (few hours before)  
214 irrigation events. In this case, many homogenous sub-plots were defined using hand-held GPS  
215 (brand: GARMIN, model: OREGON 550, location precision < 2m). The soil moisture was  
216 approximately 12 Vol.% when the plot was not supplied by water (irrigation or rainfalls) for 10  
217 days during the summer, and it reached approximately 45 Vol.% approximately 10 hours after  
218 irrigation ended. The standard deviation of soil moisture measurements within a plot was  
219 between 1 and 5 Vol.%.

220 Soil roughness measurements were conducted only once because soil roughness remains  
221 stable, using a needle profile-meter (total length of 1 m, and needle spacing of 2 cm). Ten  
222 roughness profiles (five parallels and five perpendiculars to SAR's line of sight) were recorded  
223 for each plot couple of days after the third harvest, when the vegetation was very short. The root

224 mean square height (*Hrms*) which represents the vertical scale of roughness, and the correlation  
225 length (*L*), representing the horizontal scale, were derived by processing the roughness profile.  
226 The individual autocorrelation functions are averaged, to produce a mean autocorrelation  
227 function representing each training plot (exponential function). Then, this mean autocorrelation  
228 function was used to derive *Hrms* and *L*. The *Hrms* values varied between 0.35 and 0.55 cm, and  
229 the correlation length (*L*) ranged from 2.00 to 4.60 cm.

#### 230 2.4.2 Vegetation parameters

231 Additionally, in situ measurement of vegetation parameters were performed to estimate the  
232 fresh Biomass (BIO), Vegetation Water Content (VWC), Vegetation Height (HVE), leaf area  
233 index (LAI), Fraction of Absorbed Photosynthetically Active Radiation (FAPAR), and Fractional  
234 vegetation COVER (FCOVER). The vegetation characteristics within each plot are relatively  
235 homogeneous. To determine the BIO, two vegetation samples over a 50 cm x 50 cm square were  
236 clipped using shears at the center of each plot, and then weighed (wet biomass). Later, these  
237 samples were dried at 70°C for three days to calculate the VWC (VWC = wet biomass – dry  
238 biomass). The VWC is well correlated to the BIO (VWC = 0.80 BIO,  $R^2=0.99$ ), it increases as  
239 BIO increases (i.e. growing season progresses). A poor correlation was found between VWC and  
240 soil moisture. Twenty measurements of vegetation heights were performed for each plot (the  
241 standard deviation of HVE measurements within a plot was between 5 and 10 cm). Finally,  
242 twenty to thirty hemispherical images were acquired for each plot by means of a fish eye lens.  
243 These photos were processed using CanEye software (<http://www6.paca.inra.fr/can-eye>) to  
244 estimate the LAI, FAPAR and FCOVER. Figure 2 showed photos for plots at different  
245 vegetation growth stage. For HVE, LAI, FAPAR, and FCOVER the measurements location  
246 within each plot were approximately evenly distributed in space (on average every 20 m). All

247 vegetation measurements within each plot were averaged to provide a mean value for each plot.

248 Figure 2 showed photos for plots at different vegetation growth stage.

249 In our study site, HVE reaches a value between 80 cm and 120 cm (BIO ~ 4.2 kg/m<sup>2</sup>, LAI ~ 5  
250 m<sup>2</sup>/m<sup>2</sup>) five to seven days before harvest. About ten days after harvest, the HVE reaches a value  
251 of about 30 cm (BIO ~0.80 kg/m<sup>2</sup>, LAI ~2.5 m<sup>2</sup>/m<sup>2</sup>).

252

	Training plot 2e (Jun 10, 2013) BIO= 0.89 kg/m <sup>2</sup> HVE = 0.25 m LAI = 1.01 m <sup>2</sup> /m <sup>2</sup>
	Training plot 1l (April 19, 2013) BIO= 1.90 kg/m <sup>2</sup> HVE = 0.50 cm LAI = 3.98 m <sup>2</sup> /m <sup>2</sup>
	Training plot 1m (May 14, 2013) BIO= 3.56 kg/m <sup>2</sup> HVE = 1.13 m LAI = 4.71 m <sup>2</sup> /m <sup>2</sup>

253 **Figure 2.** Ground-based photographs of study sites illustrating variations in grass growth stages  
254 along with in situ measurements.

255

256 The *in situ* campaigns, frequently performed along each of the three growth cycles, capture  
 257 full range of soil moisture and vegetation conditions (Table 2). Table 2 shows the number of  
 258 sampled plots that correspond to soil and vegetation conditions.

259 **Table 2 :** The number of sampled plots for each soil moisture and vegetation conditions

	Low (HVE $\leq$ 25 cm)	Medium (25 < HVE $\leq$ 60 cm)	High (HVE > 60 cm)
Low ( $M_v \leq 20$ Vol.%)	10	17	13
Medium (20 < $M_v \leq 30$ Vol.%)	19	40	20
High ( $M_v > 30$ Vol.%)	20	21	18
	Low (VWC $\leq$ 0.7 kg/m <sup>2</sup> )	Medium (0.7 < VWC $\leq$ 1.3 kg/m <sup>2</sup> )	High (VWC > 1.3 kg/m <sup>2</sup> )
Low ( $M_v \leq 20$ Vol.%)	12	13	15
Medium (20 < $M_v \leq 30$ Vol.%)	30	26	23
High ( $M_v > 30$ Vol.%)	20	22	17

260

### 261 3. Methods

#### 262 3.1 Radar signal modeling

263 In this study, the Water Cloud model (WCM), developed by Attema and Ulaby (1978), was  
 264 used for modeling the total backscattered radar signal according to soil moisture and vegetation  
 265 parameters. This semi-empirical model is widely used over soil with vegetation cover because it  
 266 can be easily performed in an inversion scheme to estimate soil moisture and vegetation  
 267 parameters (Gherboudj et al., 2011; Prevot et al., 1993; De Roo et al., 2001; Sikdar and  
 268 Cumming, 2004; Soon-Koo Kweon et al., 2012; Wang et al., 2011; Yang et al., 2012; Yu and  
 269 Zhao, 2011; Zribi et al., 2011). The significant variables in the WCM are the medium height and

270 dielectric cylinder density (Attema and Ulaby, 1978). The latter was assumed to be proportional  
 271 to the volumetric water content of the canopy. Very few studies have compared different  
 272 vegetation parameters to define the optimal one for use in the WCM. Champion (1991) and  
 273 Champion and Guyot (1991) found that the LAI (m<sup>2</sup>/m<sup>2</sup>) better represents the wheat canopy in  
 274 the WCM than the VWC per unit volume (kg/m<sup>3</sup>). Said *et al.* (2012) compared the use of LAI  
 275 (m<sup>2</sup>/m<sup>2</sup>), VWC (kg/m<sup>2</sup>), and HVE and found that the use of LAI as the vegetation descriptor  
 276 allows the accurate simulation of the vegetation volume contribution (sugarcane, cherry, rice,  
 277 and grassland).

278 In this context, the WCM represents the total backscattered radar signal ( $\sigma^0_{\text{tot}}$ ) in linear scale  
 279 as a sum of the direct vegetation contribution ( $\sigma^0_{\text{veg}}$ ) and soil contribution attenuated by the  
 280 vegetation volume ( $T^2 \sigma^0_{\text{sol}}$ ).

$$\sigma^0_{\text{tot}} = \sigma^0_{\text{veg}} + T^2 \sigma^0_{\text{sol}} \quad (\text{Eq. 4})$$

$$\sigma^0_{\text{veg}} = A.V_1.\cos \theta (1 - T^2) \quad (\text{Eq. 5})$$

$$T^2 = \text{Exp} (-2.B.V_2.\sec \theta) \quad (\text{Eq. 6})$$

$$\sigma^0_{\text{sol}} = C(\theta) \exp (D.M_v) \quad (\text{Eq. 7})$$

281

282

283 Where:

- 284 •  $V_1$  and  $V_2$  are vegetation descriptors (BIO ( $\text{kg}/\text{m}^2$ ), VWC ( $\text{kg}/\text{m}^2$ ), HVE (m), LAI  
285 ( $\text{m}^2/\text{m}^2$ ), FAPAR, FCOVER, and NDVI)
- 286 •  $\theta$  is the radar incidence angle
- 287 • A and B are parameters that depend on the canopy descriptors and radar  
288 configurations
- 289 •  $T^2$  is the two way attenuation
- 290 • C is dependent on the roughness and incidence angle
- 291 • D is the sensitivity of the radar signal to volumetric soil moisture in the case of  
292 bare soils, which is dependent on radar configurations
- 293 •  $M_v$  is the volumetric soil moisture (expressed in Vol.%).

294

### 295 3.2 Soil moisture retrieval

296 In this study, soil moisture was estimated by means of multi-layer perceptron neural networks  
297 (NNs). The Levenberg-Marquardt optimization algorithm (Marquardt, 1963) was used to train  
298 the NNs. The NNs architecture is composed of three layers: input, one hidden, and output. The  
299 NNs have a two dimensional input vector when using one polarization (HH or HV) in addition to  
300 one vegetation descriptor. Using two polarizations (HH and HV) in addition to one vegetation  
301 descriptor, the NNs have a three dimensional input vector. The one dimensional output vector  
302 contains soil moisture. The numbers of neurons associated with the hidden layer was determined  
303 by training the NNs using different numbers of neurons. 20 hidden neurons provided accurate  
304 estimates of reference parameters (Baghdadi et al., 2012a; Chai et al., 2009). Sigmoidal and  
305 linear transfer functions were associated with the hidden and output layer, respectively. These

306 functions allow non-linear transformations from input to output (Del Frate and Solimini, 2004;  
307 Del Frate et al., 2003; Paloscia et al., 2008). To study the performance of the inversion approach,  
308 the NNs were trained and validated on the synthetic datasets.

309 A Synthetic dataset of SAR backscatter data was generated from the parameterized WCM to  
310 be used in the procedures leading to the estimation of soil moisture by means of the neural  
311 networks (NNs) technique. The parameterized WCM is able to simulate the backscattering  
312 coefficients at both HH and HV polarizations using the volumetric soil moisture, one vegetation  
313 descriptor, and incidence angle values as input variables. Only parameters easily estimated from  
314 optical images such as NDVI, LAI, FAPAR and FCOVER were considered in the synthetic  
315 datasets generation. Indeed, only few studies showed that the optical data could be used for  
316 estimating the biomass, vegetation water content, and the vegetation height. Four synthetic  
317 datasets have thus been generated using NDVI, LAI, FAPAR and FCOVER as vegetation  
318 descriptors (V1 and V2 in equations 4 and 5) to evaluate the most adequate vegetation descriptor  
319 for vegetation layer characterization in the WCM, and to open a perspective for future works  
320 based on SAR and optical data coupling. Indeed, several studies have developed methods to  
321 correct atmospheric effects in optical images, allowing the accurate estimation of the NDVI  
322 (Agapiou et al., 2011; Masek et al., 2013; Rahman and Dedieu, 1994; Saastamoinen, 1972;  
323 Vermote et al., 2002). Regarding the other vegetation descriptors, many studies have developed  
324 methods to estimate LAI, FAPAR, and FCOVER from optical images (Baret and Guyot, 1991;  
325 Bsaibes et al., 2009; Carlson and Ripley, 1997; Carlson et al., 1994; Claverie et al., 2013;  
326 Courault et al., 2008; Darvishzadeh et al., 2008b; Duveiller et al., 2011; Fensholt et al., 2004;  
327 Guerschman et al., 2009; Li et al., 2014; North, 2002). In addition, in the framework of our  
328 study, LAI, FAPAR, and FCOVER of our studied grassland were derived from optical images

329 (SPOT-4, SPOT-5, LANDSAT-7, LANDSAT-8) using the BV-NNET (Biophysical Variables  
 330 Neural NETWORK) tool developed based on algorithms proposed by Baret *et al.* (2007) and then  
 331 optimized through the SIRRIMED project (<http://www.sirrimed.org/index.php>). A comparison  
 332 was performed between the LAI, FAPAR and FCOVER derived from BV-NNET (using optical  
 333 images) and those derived from hemispherical photos. Results showed unbiased estimations of  
 334 LAI, FAPAR, and FCOVER by the BV-NNET. Moreover, the BV-NNET estimates the LAI  
 335 with an RMSE of 0.66 m<sup>2</sup>/m<sup>2</sup> and an RRMSE (as well as MAPE) around 29%. For FAPAR and  
 336 FCOVER, an RMSE around 0.13 and an RRMSE (as well as MAPE) around 19% were obtained.

337 The synthetic dataset based on NDVI as the vegetation descriptor comprises 80 elements (8 x  
 338 10, Table 3). Each element of the dataset contains radar signals in HH and HV polarizations for a  
 339 given NDVI and volumetric soil moisture (Table 3). Moreover, synthetic dataset based on LAI  
 340 and FAPAR (as well as FCOVER) comprised 248 (8 x 31, table 3) and 168 (8 x 21, table 3)  
 341 elements, respectively.

342 **Table 3.** The minimum, maximum, and step values of WCM inputs.

<b>Parameter</b>	<b>Min value</b>	<b>Max value</b>	<b>Step</b>	<b>Total elements</b>
<b>NDVI</b>	0.45	0.90	0.05	10
<b>LAI (m<sup>2</sup>/m<sup>2</sup>)</b>	0.0001	6	0.20	31
<b>FAPAR</b>	0.0001	1	0.05	21
<b>FCOVER</b>	0.0001	1	0.05	21
<b>M<sub>v</sub> (Vol.%)</b>	10	45	5	8

343 To make WCM simulations more realistic, uncertainties of SAR measurements were added to  
344 the simulated radar response. The uncertainties range is between 0.6 and 1 dB for CSK and TSX  
345 sensors (Agenzia Spaziale Italiana, 2007; Coletta et al., 2007; Iorio et al., 2010; Schwerdt et al.,  
346 2008; Torre et al., 2011). Thus, we considered two absolute uncertainties values ( $\pm 0.75$ , and  
347  $\pm 1.00$  dB) to be added to the simulated radar response. Moreover, relative uncertainties were  
348 added on our reference vegetation descriptor values (NDVI, LAI, FAPAR, and FCOVER) to  
349 handle the associated uncertainty. For NDVI, Simoniello *et al.* (2004) reported a relative  
350 uncertainty of approximately 8% on NDVI values estimated from AVHRR (Advanced Very  
351 High Resolution Radiometer) calibrated data over pasture and cultivated areas. El Hajj *et al.*  
352 (2008) found that the relative uncertainty on NDVI computed from SPOT-5 surface reflectance  
353 data over sugarcane fields is approximately 13%. For the other vegetation descriptors, studies  
354 showed for crop canopies (corn, grass, sunflower, maize, wheat, rapeseed and sunflower) relative  
355 uncertainty between 10% and 30% for LAI, and between 5% and 20% for FAPAR and FCOVER  
356 (Bsaibes et al., 2009; Claverie et al., 2013; Courault et al., 2008; Duveiller et al., 2011; North,  
357 2002). In addition, the uncertainty on the vegetation descriptor estimates depends on crop type  
358 (Bsaibes et al., 2009; Claverie et al., 2013). Moreover, the comparison between derived LAI,  
359 FAPAR, and FCOVER from our optical images with ground-truthed measurements yields a  
360 relative RMSE (Root Mean Square Error) of 29.12, 19.24, and 18.14%, respectively. Therefore,  
361 in our study we considered a relative additive noise of 15, 30, and 20% on the NDVI, LAI, and  
362 FAPAR (as well as FCOVER), respectively.

363 Zero-mean Gaussian noise with a standard deviation equal to absolute and relative  
364 uncertainties were added to the radar signal simulated by the WCM and reference vegetation  
365 descriptors, respectively. Finally, to obtain statistically significant datasets, 500 random

366 samplings of zero-mean Gaussian noise was added to each simulated radar response and each  
367 vegetation descriptor value.

368 Three case studies to estimate soil moisture using X-band SAR data were evaluated:

- 369 • Case 1: Noisy radar signal at HH polarization and noisy vegetation descriptor as the  
370 inputs to NNs, and soil moisture as the target.
- 371 • Case 2: Noisy radar signal at HV polarization and noisy vegetation descriptor as the  
372 inputs to NNs, and soil moisture as the target.
- 373 • Case 3: Noisy radar signal at HH and HV polarizations and noisy vegetation descriptor as  
374 the inputs to NNs, and soil moisture as the target.

375 Finally, the calibrated NNs were used to invert real SAR measurements for estimation of the  
376 soil moisture. The inversion was performed according to the configurations above, but using  
377 SAR and a vegetation descriptor (LAI, FAPAR, and FCOVER) derived from optical images  
378 instead of the noisy radar signal and vegetation descriptors.

## 379 **4. Results and discussions**

### 380 4.1 Water Cloud Model parameterization, and modelling results

381 This section presents the results of the Water Cloud Model (WCM) parameterization, and shows  
382 the radar signal modelling results as a function of soil and vegetation parameters.

#### 383 4.1.1 Water Cloud Model parameterization

384 The real dataset composed of SAR data and measurements of soil moisture and vegetation  
385 descriptors was divided into two sub-datasets. The first sub-dataset (training dataset) was used to  
386 fit the WCM model, whereas the second (validation dataset) was used to validate the soil

387 moisture estimation of the WCM model. The training dataset contains the SAR and the ground-  
388 truthed data obtained during the three cycles for the half of training plots, whereas the validation  
389 dataset comprises the data collected for other half of plots. These two real sub-datasets contain a  
390 wide range of soil moisture ( $M_v$ ) and vegetation descriptor values measured in situ (BIO, VWC,  
391 HVE, LAI, FAPAR, FCOVER) and derived from optical images (NDVI, LAI, FAPAR, and  
392 FCOVER) (Table 4). The two real sub-datasets have almost the same ranges of variation.

393

394

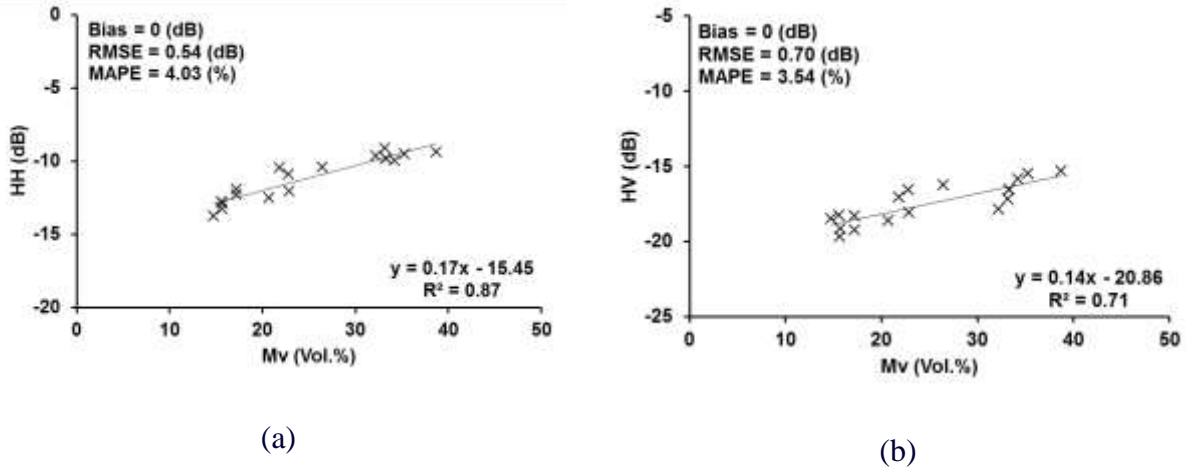
**Table 4:** ranges of variation of real training and validation datasets

Real training dataset		Min	Mean	MAX	Unit
	Mv	10.9	25.6	39.0	Vol.%
	In situ BIO	0.28	1.41	4.14	Kg/m <sup>2</sup>
	In situ VWC	0.15	1.12	3.35	Kg/m <sup>2</sup>
	In situ HVE	0.08	0.48	1.20	m
	In situ LAI	0.10	2.64	5.88	m <sup>2</sup> /m <sup>2</sup>
	In situ FAPAR	0.20	0.79	1.00	-
	In situ FCOVER	0.12	0.63	0.96	-
	LAI (BV-NNET)	0.20	2.63	5.04	m <sup>2</sup> /m <sup>2</sup>
	FAPAR (BV-NNET)	0.16	0.77	0.98	-
	FCOVER (BV-NNET)	0.16	0.66	0.96	-
NDVI	0.47	0.73	0.88	-	
Real validation dataset					
	Mv	14.1	27.0	47.0	Vol.%
	In situ BIO	0.30	1.31	3.46	Kg/m <sup>2</sup>
	In situ VWC	0.03	1.02	2.87	Kg/m <sup>2</sup>
	In situ HVE	0.08	0.45	1.15	m
	In situ LAI	0.26	2.23	4.00	m <sup>2</sup> /m <sup>2</sup>
	In situ FAPAR	0.20	0.73	0.93	-
	In situ FCOVER	0.09	0.57	0.88	-
	LAI (BV-NNET)	0.26	2.16	5.10	m <sup>2</sup> /m <sup>2</sup>
	FAPAR (BV-NNET)	0.09	0.69	0.98	-
	FCOVER (BV-NNET)	0.09	0.58	0.94	-
NDVI	0.48	0.69	0.87	-	

395 WCM parameterization consists of first estimating the sensitivity parameter D before fitting  
396 the model against ground-truthed measurements to estimate parameters A, B, and C (equations 4,  
397 5, and 6).

398 • To estimate parameter D, SAR backscattering coefficients in HH and HV  
399 polarizations (dB scale) were linearly related to soil moisture (Vol.%) for 18 plots  
400 recently harvested (vegetation very short), to have the minimum vegetation effect on  
401 the backscattering coefficients (Figure 3). The slopes of these linear regressions  
402 represent the sensitivity of the backscattered radar signal to volumetric soil moisture  
403 on the dB scale (Figure 3). Results showed a good correlation between radar signal  
404 and volumetric soil moisture ( $R^2 = 0.87$  and  $0.71$  for HH and HV, respectively).  
405 Moreover, results showed that the HH polarization is slightly more sensitive ( $0.172$   
406 dB/Vol.%) to volumetric soil moisture rather than HV ( $0.135$  dB/Vol.%) polarization  
407 (Figure 3). In the WCM model, the sensitivity parameter D is represented on a linear  
408 scale. In linear unit, these sensitivities  $D_{HH}$  and  $D_{HV}$  are  $0.03971$  [ $m^2/m^2$ ]/[Vol.%] and  
409  $0.03116$  [ $m^2/m^2$ ]/[Vol.%] for HH and HV polarizations, respectively

410 • A, B and C parameters were then estimated for each radar polarization and each  
411 vegetation descriptor (NDVI and ground-truthed BIO, VWC, HVE, LAI, FAPAR, and  
412 FCOVER) by minimizing the sum of squares of the differences between the simulated  
413 and measured radar signal. Therefore, the WCM was parameterized according to  
414 seven vegetation descriptors (Table 5). With A, B and C parameters, it becomes  
415 possible to predict WCM components ( $\sigma_{veg}^0$ ,  $T^2$ , and  $\sigma_{sol}^0$ ) and consequently the total  
416 backscattering coefficient ( $\sigma_{tot}^0$ ) using one vegetation descriptor and the soil moisture  
417 values as inputs in the WCM.



418 **Figure 3.** Sensitivity of radar signal in both HH and HV polarization to volumetric soil moisture.  
 419

420 To validate the fitted WCM, a comparison was performed between the radar backscattering  
 421 coefficients predicted by the mean of the parameterized WCM (using the soil moisture and  
 422 ground-truthed vegetation descriptors of the real validation dataset) and the observed  
 423 backscattering coefficients of the real validation dataset. Results showed that the fit of the WCM  
 424 was slightly better in HH polarization than in HV polarization (Table 5). The limited correlation  
 425 coefficient ( $R^2$ ) is not due to difficulty of model to simulate radar data but particularly to limited  
 426 range of radar data dynamic for different moisture and vegetation conditions. In addition, the  
 427 quality of the fit is approximately the same for all the used vegetation descriptors with the RMSE  
 428 (Root Mean Square Error) on the predicted backscattering coefficients between 0.76 and 0.86 dB  
 429 in HH, and between 0.85 and 0.94 dB in HV polarization, depending on the used vegetation  
 430 descriptor. Water cloud model is considered adequately fitted because the RMSE on simulated  
 431 radar signal in both HH and HV polarizations is less than 1 dB, which is the same magnitude as  
 432 the CSK and TSX sensors precision (Agenzia Spaziale Italiana, 2007; Coletta et al., 2007; Iorio  
 433 et al., 2010; Schwerdt et al., 2008; Torre et al., 2011). Several studies used the WCM model to  
 434 predict radar backscattering coefficients (Attema and Ulaby, 1978; Gherboudj et al., 2011;

435 Prevot et al., 1993; Ulaby et al., 1984). Attema and Ulaby, (1978) simulated the X-band  
436 backscattering coefficients for crops fields (alfalfa, corn, milo, and wheat) in HH and VV  
437 polarizations for a wide range of incidence angles ( $0^{\circ}$ - $70^{\circ}$ ) with a RMSE of simulated  
438 backscattering coefficients ranging between 1.5 and 2 dB, depending on the crop type. Ulaby *et*  
439 *al.*, (1984) simulated the radar backscattering coefficients in the X-band (VV polarization and  $50^{\circ}$   
440 incidence angle) for wheat fields with a RMSE of 1.6 dB. Prevot *et al.* (1993) obtained a RMSE  
441 for wheat fields on the simulated backscattering coefficients of 1.24 and 0.72 dB in the C-band  
442 (HH,  $20^{\circ}$ ) and X-band (VV,  $40^{\circ}$ ), respectively. Gherboudj et al. (2012) predicted the  
443 backscattering coefficients in the C-band, in quad-polarization mode with a  $30^{\circ}$  incidence angle  
444 for wheat and pea fields. The RMSE on the predicted backscattering coefficients in HH and VV  
445 polarizations was approximately 1 (for wheat) and 0.7 dB (for peas), respectively. In cross  
446 polarization, the backscattering coefficient was simulated with a RMSE of 1.2 and 0.2 dB for  
447 wheat and pea fields, respectively.

448

**Table 5.** Fit of WCM parameters for HH and HV polarizations (real validation dataset).

<b>V1=V2</b>	<b>A<sub>HH</sub></b>	<b>B<sub>HH</sub></b>	<b>C<sub>HH</sub></b>	<b>D<sub>HH</sub></b>	<b>A<sub>HV</sub></b>	<b>B<sub>HV</sub></b>	<b>C<sub>HV</sub></b>	<b>D<sub>HV</sub></b>	<b>R<sup>2</sup><sub>HH</sub> (R<sup>2</sup><sub>HV</sub>)</b>	<b>RMSE<sub>HH</sub> (RMSE<sub>HV</sub>) (dB)</b>
<b>Ground-truthed BIO</b>	0.0345	0.0995	0.0334	0.03971	0.0068	0.1850	0.0093	0.03116	0.49 (0.39)	0.85 (0.86)
<b>Ground-truthed VWC</b>	0.0438	0.1047	0.0324	0.039711	0.0084	0.1927	0.0088	0.03116	0.49 (0.39)	0.86 (0.86)
<b>Ground-truthed HVE</b>	0.1045	0.4314	0.0357	0.03971	0.0207	0.7882	0.0105	0.03116	0.52 (0.40)	0.79 (0.85)
<b>Ground-truthed LAI</b>	0.0205	0.0613	0.0338	0.03971	0.0041	0.0856	0.0088	0.03116	0.48 (0.29)	0.86 (0.95)
<b>Ground-truthed FAPAR</b>	0.0911	0.3275	0.0354	0.03971	0.0177	0.4662	0.0096	0.03116	0.47 (0.25)	0.80 (0.93)
<b>Ground-truthed FCOVER</b>	0.1021	0.3696	0.0355	0.03971	0.0203	0.5212	0.0095	0.03116	0.48 (0.27)	0.82 (0.94)
<b>NDVI</b>	0.0767	0.7944	0.0644	0.03971	0.016474	1.134	0.0221	0.03116	0.51 (0.33)	0.76 (0.93)

450

451

## 4.1.2 Modelling results

452

453

454

455

456

Modelling results obtained by using the NDVI as the vegetation descriptor in the WCM model will be presented first because (i) the best fit of water cloud model was obtained with NDVI as vegetation descriptor, and (ii) it is easier to derive NDVI from optical data than LAI, FAPAR, and FCOVER. Next, results with the LAI, FAPAR, FCOVER, BIO, VWC, and HVE as vegetation descriptors will be briefly discussed.

457 The WCM components ( $T^2\sigma_{sol}^\circ$  and  $\sigma_{veg}^\circ$ ) were simulated for wide ranges of soil moisture  
 458 ( $M_v$ ) and NDVI values using the WCM with the NDVI as the vegetation descriptor. For both HH  
 459 and HV polarizations, the vegetation contribution ( $\sigma_{veg}^\circ$ ), soil contribution ( $\sigma_{sol}^\circ$ ), two-way  
 460 attenuation ( $T^2$ ), and consequently, the total backscattered signal ( $\sigma_{tot}^\circ$ ) were generated in a linear  
 461 scale using the parameterized equations (3) to (6). NDVI values ranging from 0.45 to 0.90 were  
 462 used to simulate the vegetation contribution and the two-way attenuation ( $V1=V2=NDVI$  in  
 463 equations 4 and 5). In addition, the soil contribution was simulated using  $M_v$ -values ranging from  
 464 10 to 45 Vol.% (equation 6). The maximum values of NDVI and  $M_v$  correspond to the highest  
 465 values derived from optical images and measured in situ, respectively.

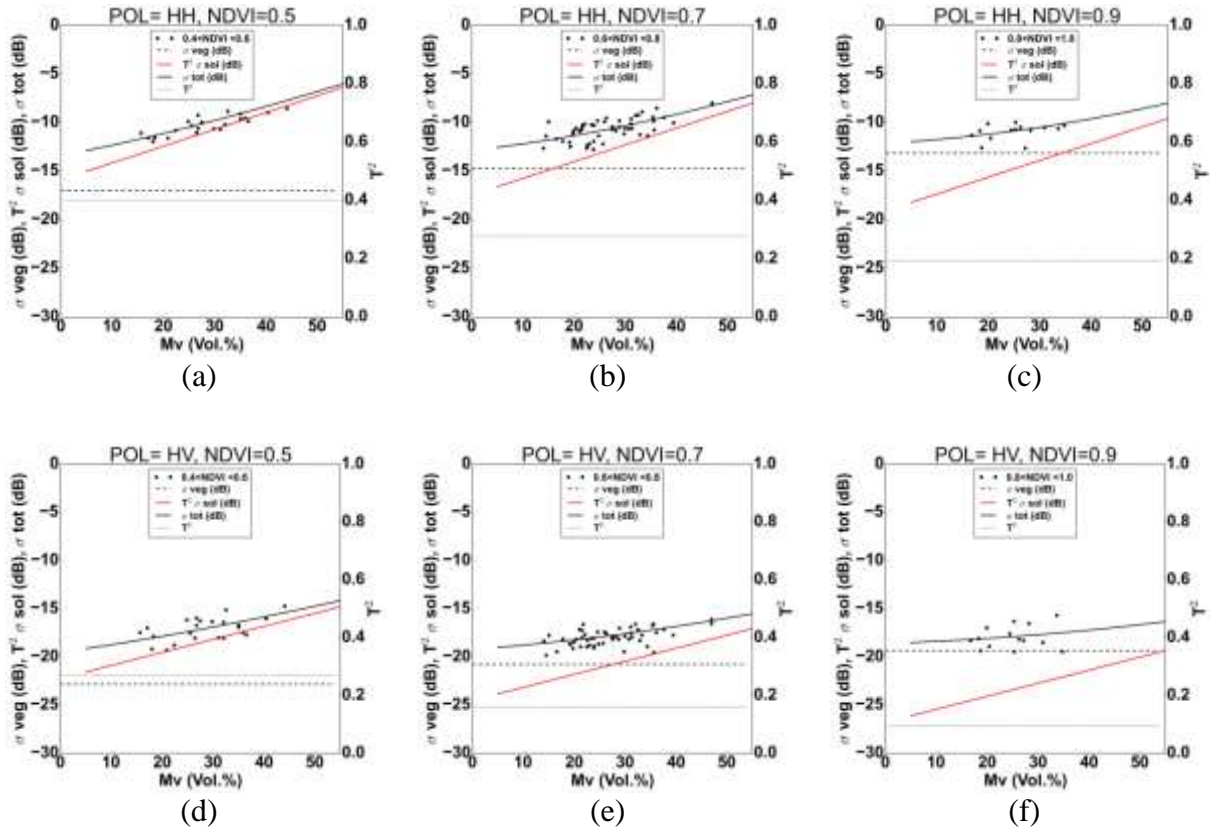
466 Figure 4 shows the modelled  $\sigma_{veg}^\circ$ ,  $T^2\sigma_{sol}^\circ$  and  $\sigma_{tot}^\circ$  in dB units as a function of  $M_v$  using  
 467 different values of NDVI (0.5, 0.7, and 0.9). In addition, the modelled  $\sigma_{veg}^\circ$ ,  $T^2\sigma_{sol}^\circ$  and  $\sigma_{tot}^\circ$   
 468 were also plotted according to NDVI for  $M_v$  values of 15, 20, 30 and 40 Vol.% (Figure 5).

469 Figure 4 shows that  $\sigma_{tot}^\circ$  in both HH and HV polarizations are always sensitive to soil  
 470 moisture even for high NDVI values. The sensitivity of  $\sigma_{tot}^\circ$  to soil moisture decreases with the  
 471 NDVI for NDVI between 0.45 and 0.90. For NDVI value equal to 0.50 this sensitivity is about  
 472 0.14 dB/% and 0.10dB/% for HH and HV, respectively. Moreover, for a NDVI value equal to  
 473 0.9, this sensitivity is approximately 0.08 and 0.04 dB/Vol.% in HH and HV, respectively. For  
 474 each case in figure 4 statistical index were provided in table 6. Results showed that the WCM  
 475 adequately simulates SAR real validation dataset observations ( $0 < Bias < 0.3$ ,  $RMSE < 1dB$ ,  
 476  $RRMSE$  and  $MAPE < 7\%$ ).

477 Figure 5 shows that  $\sigma_{tot}^\circ$  in both HH and HV polarization is slightly sensitive to the NDVI (for  
 478 NDVI between 0.45 and 0.90). Indeed, as the vegetation grows, the decreasing soil contribution  
 479 is similar to the increasing vegetation contribution.  $\sigma_{tot}^\circ$  shows slight decreases with increases in

480 the NDVI until reaching a minimum, and starts to slightly increase. In both HH and HV  
481 polarizations,  $\sigma^{\circ}_{\text{tot}}$  decreases with NDVI for a NDVI lower than 0.60, 0.75, and 0.90 for  $M_v$  of  
482 15, 20, and 30 Vol.%, respectively. However, the  $\sigma^{\circ}_{\text{tot}}$  in both HH and HV polarizations always  
483 decreases with NDVI (NDVI between 0.45 and 0.90) for  $M_v$  equal to 40 Vol.% due to the high  
484 soil contribution (Figures 5 d and h). This decrease of  $\sigma^{\circ}_{\text{tot}}$  with the NDVI is related to an  
485 increase in the attenuation of the soil contribution ( $T^2$ ), which is more important than the  
486 enhanced contribution from the vegetation canopy (Balenzano et al., 2011; Brown et al., 2003;  
487 Mattia et al., 2003). Beyond these values of NDVI thresholds,  $\sigma^{\circ}_{\text{tot}}$  increases slightly with NDVI  
488 for  $M_v$  values between 15 and 30 Vol.%. This increase of  $\sigma^{\circ}_{\text{tot}}$  with NDVI results in the increase  
489 of the vegetation contribution combined with the decrease in the soil contribution. Moreover, the  
490 decrease and increase of  $\sigma^{\circ}_{\text{tot}}$  according to the NDVI are slightly more pronounced in HV than in  
491 HH polarization. Regarding vegetation contribution ( $\sigma^{\circ}_{\text{veg}}$ ), results showed that the modelled  
492  $\sigma^{\circ}_{\text{veg}}$  in HH polarization increases from -17.7 dB for NDVI of 0.45 to -13.2 dB for NDVI of 0.90.  
493 For HV polarization,  $\sigma^{\circ}_{\text{veg}}$  increases from -23.5 dB to -18.8 dB for NDVI between 0.45 and 0.90.  
494 For each case in figure 5, statistical index were provided in table 7. Results showed that the  
495 WCM adequately simulates SAR real validation dataset observations ( $0 < \text{Bias} < 0.7$ ,  $\text{RMSE} \leq$   
496  $1\text{dB}$ ,  $\text{RRMSE}$  and  $\text{MAPE} < 8\%$ ).

497

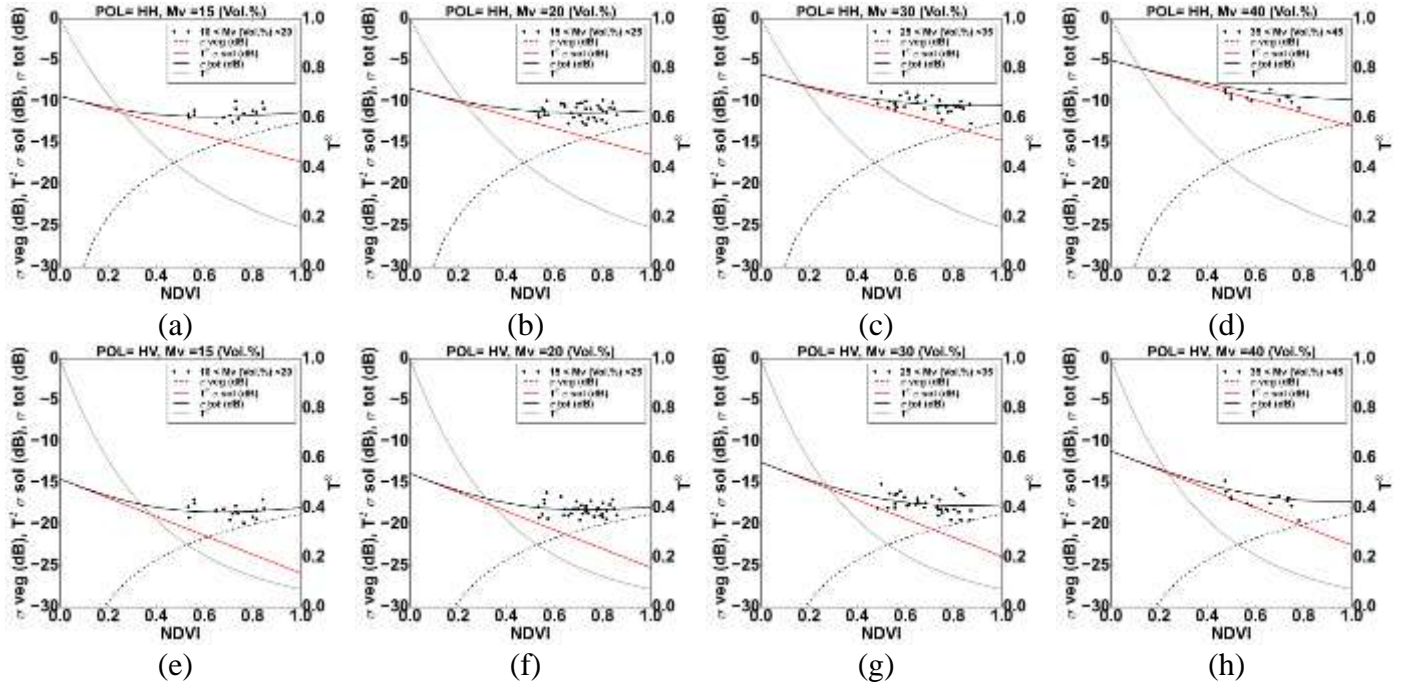


498 **Figure 4.** Behavior of WCM components ( $\sigma^{\circ}_{veg}$ ,  $T^2\sigma^{\circ}_{sol}$ , and  $\sigma^{\circ}_{tot}$ ) in both HH and HV  
 499 polarizations according to  $M_v$ . Black points represent the SAR data ( $\sigma^{\circ}_{tot}$ : real validation dataset)  
 500 associated with NDVI measurements within  $\pm 0.1$  of the NDVI used in the modelling.

501 **Table 6:** Statistical index for each case in figure 4

Case	Polarization	NDVI	Bias (dB)	RMSE (dB)	RRMSE (dB)	MAPE (dB)	$R^2$	Nb
Figure 4a	HH	0.50	0.3	0.6	6.0	5.4	0.71	23
Figure 4b	HH	0.70	0.0	0.9	8.0	6.7	0.45	52
Figure 4c	HH	0.90	0.1	0.8	7.0	4.8	0.12	14
Figure 4d	HV	0.50	0.1	1.0	5.7	5.1	0.30	23
Figure 4e	HV	0.70	0.2	0.8	4.3	3.3	0.26	52
Figure 4f	HV	0.90	0.1	1.1	6.4	5.5	0.03	14

502



503 **Figure 5.** Behavior of WCM components ( $\sigma_{veg}^{\circ}$ ,  $T^2\sigma_{sol}^{\circ}$ , and  $\sigma_{tot}^{\circ}$ ) in both HH and HV  
 504 polarizations according to NDVI. Black points represent the SAR data ( $\sigma_{tot}^{\circ}$ : real validation  
 505 dataset) associated with  $M_v$  measurements within  $\pm 5$  vol. % of the  $M_v$  used in the modelling.

506 **Table 7:** Statistical index for each case in figure 5

Case	Polarization	$M_v$ (Vol.%)	Bias (dB)	RMSE (dB)	RRMSE (%)	MAPE (%)	$R^2$	Nb
Figure 5a	HH	15	-0.3	0.8	6.8	5.6	0.13	17
Figure 5b	HH	20	-0.1	0.9	7.7	6.7	0.00	36
Figure 5c	HH	30	0.1	0.7	7.1	5.4	0.16	37
Figure 5d	HH	40	0.6	0.8	8.7	7.6	0.32	12
Figure 5e	HV	15	-0.1	0.8	4.3	3.6	0.05	17
Figure 5f	HV	20	0.0	0.8	4.5	3.7	0.01	36
Figure 5g	HV	30	0.1	1.0	5.5	4.7	0.18	37
Figure 5h	HV	40	0.6	1.1	6.3	5.0	0.41	12

507 Table 8 shows NDVI thresholds from which the  $T^2\sigma_{sol}^{\circ}$  is dominated by  $\sigma_{veg}^{\circ}$  ( $T^2\sigma_{sol}^{\circ} < \sigma_{veg}^{\circ}$ ).  
 508 In HH polarization, these thresholds are approximately 0.69, 0.74, 0.85, 0.97 for soil moisture of

509 15, 20, 30 and 40 Vol.%, respectively. In HV polarizations and for  $M_v$  values of 15, 20, 30 and  
 510 40 Vol.%,  $\sigma^{\circ}_{veg}$  dominates  $T^2\sigma^{\circ}_{sol}$  for NDVI values greater than 0.62, 0.65, 0.71, and 0.79,  
 511 respectively. Thus, for a given soil moisture value, the thresholds of NDVI for which the  
 512 vegetation contribution dominates the soil contribution are lower in HV than in HH (Table 8).

513 **Table 8.** Threshold values of vegetation descriptors at which  $\sigma^{\circ}_{veg}$  dominates  $T^2\sigma^{\circ}_{sol}$  at both HH  
 514 and HV polarizations. Dash symbols mean that the  $\sigma^{\circ}_{veg}$  is always dominated by  $T^2\sigma^{\circ}_{sol}$ .

$M_v$ (Vol.%)	HH polarization				HV polarization			
	15	20	30	40	15	20	30	40
<b>NDVI</b>	0.69	0.74	0.85	0.97	0.62	0.65	0.71	0.79
<b>LAI (m<sup>2</sup>/m<sup>2</sup>)</b>	4.22	4.60	5.43	-	3.69	3.94	4.47	5.05
<b>FAPAR</b>	0.87	0.95	-	-	0.77	0.82	0.93	-
<b>FCOVER</b>	0.78	0.84	0.99	-	0.68	0.72	0.82	0.92
<b>BIO (kg/m<sup>2</sup>)</b>	2.55	2.77	3.28	3.85	1.95	2.07	2.34	2.64
<b>VWC (kg/m<sup>2</sup>)</b>	2.20	2.40	2.84	3.35	1.70	1.82	2.06	2.32
<b>HVE (m)</b>	0.70	0.76	0.90	-	0.55	0.58	0.65	0.73

515 WCM components were also modelled using the LAI, FAPAR, FCOVER, BIO, VWC and  
 516 HVE as vegetation descriptors. Similar results on the behavior of modelled total backscattered  
 517 radar signal ( $\sigma^{\circ}_{tot}$ ) were obtained with all vegetation descriptors. Table 8 shows the values of the  
 518 vegetation descriptors at which  $\sigma^{\circ}_{veg}$  dominates  $T^2\sigma^{\circ}_{sol}$ . As an example, for soil moisture of 20  
 519 Vol.%,  $\sigma^{\circ}_{veg}$  in HH polarization dominates  $T^2\sigma^{\circ}_{sol}$  for LAI values higher than 4.60 m<sup>2</sup>/m<sup>2</sup>. In  
 520 addition, for some soil moisture and vegetation descriptor conditions, the vegetation contribution  
 521 is always dominated by the soil contribution (dash symbol in Table 8). As an example, for soil

522 moisture of 40 Vol.%, the vegetation contribution in HH polarization is always dominated by the  
523 soil contribution for HVE values between 0 and 1.2 m (maximum value of HVE obtained by  
524 ground-truthed measurements and used in modelling). In addition, Table 8 shows that the  
525 vegetation contribution in HV polarization dominates the soil contribution at threshold values of  
526 vegetation descriptors which are lower than those observed in HH polarization.

#### 527 4.2 Soil moisture retrieval

528 Synthetic and real datasets were used to estimate the soil moisture for the three inversion  
529 configurations defined in section 3.2: (1) using the radar signal in HH and one vegetation  
530 descriptor, (2) using the radar signal in HV and one vegetation descriptor, and (3) using the radar  
531 signal in both HH and HV and one vegetation descriptor. The estimated soil moistures were  
532 compared to reference soil moisture values to evaluate the accuracy of the soil moisture  
533 estimates of each inversion configuration.

534 Before the use of neural networks for soil moisture estimation, the WCM model was  
535 numerically inverted. For some points of the synthetic and real datasets where the SAR  
536 backscattering coefficient is lower than the vegetation contribution simulated by the WCM, the  
537 direct inversion of the WCM is not numerically possible (about 10% of the datasets). Such  
538 limitation is overcome when using the NNs for both synthetic and real datasets. In addition, the  
539 Root Mean Square Error on  $M_v$  estimates was better with the NNs than using the direct inversion  
540 of the WCM (precision on  $M_v$  two times better). For these reasons, the neural networks inversion  
541 technique for soil moisture estimation was considered.

542 To estimate the soil moisture, neural networks were built for each inversion configuration  
543 using a part of the synthetic dataset. The quality of inversion approaches were studied using both  
544 the other part of the synthetic dataset and the real validation dataset.

#### 545 4.2.1 Synthetic dataset

546 The synthetic dataset was composed of  $2 \cdot 10^7$  elements (10 NDVI values x 8  $M_v$  values x 500  
547 random sampling values of the NDVI x 500 random sampling values of the simulated radar  
548 signal). According to the radiometric accuracy of the TerraSAR-X and COSMO-SkyMed  
549 signals, the radar signal simulated by the WCM model was noised using an additive Gaussian  
550 noise with zero mean and a standard deviation of 0.75 and 1 dB. The synthetic dataset was  
551 randomly divided into 80% training and 20% validation data samples. The prediction error based  
552 on a 5-fold cross-validation was estimated for each inversion configuration to assess the  
553 performance of the neural networks. Analysis of the results obtained with NDVI as the  
554 vegetation descriptor will be provided in detail whereas the results based on LAI, FAPAR, and  
555 FCOVER as the vegetation descriptors will be briefly described.

556 The Root Mean Square Error (RMSE), the Relative Root Mean Square Error (RRMSE), the  
557 Mean Absolute Percentage Error (MAPE), the associated mean deviation (bias = estimated  $M_v$  -  
558 reference  $M_v$ ), and the correlation coefficient ( $R^2$ ) were used to evaluate the performance of each  
559 inversion configuration. Table 9 presents statistical indexes (RMSE, RRMSE, MAPE, bias, and  
560  $R^2$ ) on  $M_v$  estimates computed from the validation dataset for reference  $M_v$  between 10 and 45  
561 Vol.% and NDVI values between 0.45 and 0.90. Table 9 shows that the RMSE (as well as  
562 RRMSE, and MAPE) on  $M_v$  estimates is lower with HH polarization than with HV polarization  
563 (configuration 1 in comparison to configuration 2, Table 9). For a noise condition on the radar  
564 signal of  $\pm 0.75$  dB, the RMSE is 4.5 Vol.% (RRMSE and MAPE about 17 %) with HH

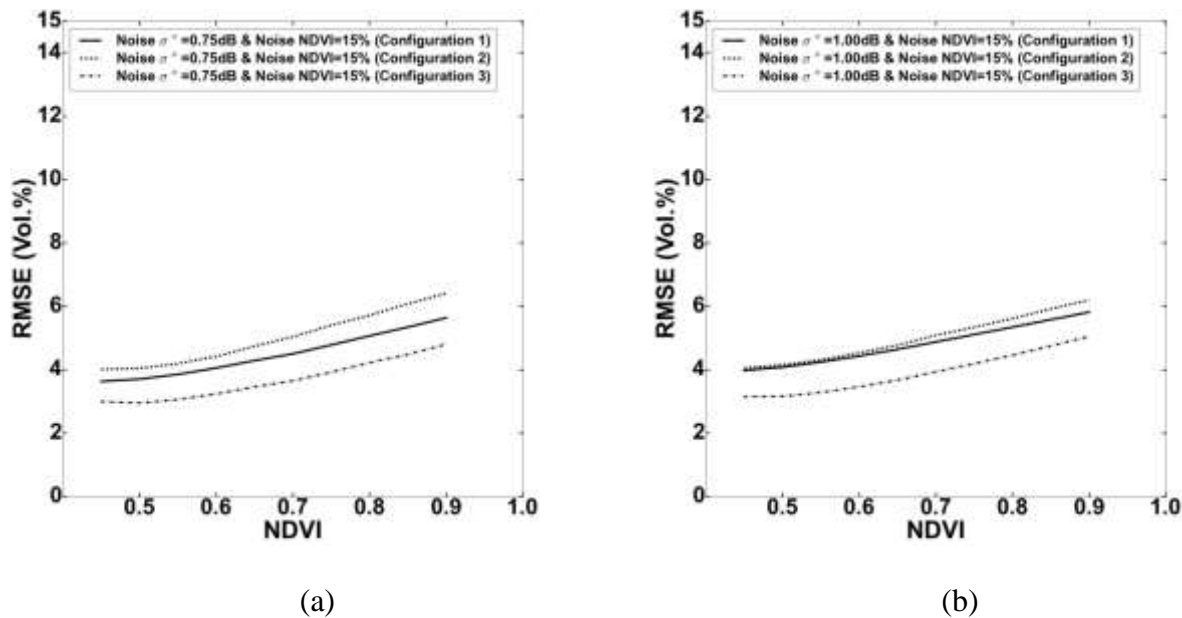
565 compared to 5.1 Vol.% (RRMSE and MAPE 19 %) with HV. In addition, results showed that the  
 566 use of both HH and HV (in addition to the NDVI, configuration 3) slightly decreases the RMSE  
 567 on  $M_v$  estimates (lower than 1 Vol.%). With configuration 3, the RMSE on  $M_v$  estimates reaches  
 568 3.7 Vol.% (RRMSE and MAPE about 14%) for a noise on the modeled radar signal of  $\pm 0.75$   
 569 (Table 9). Table 9 also shows that the RMSE on  $M_v$  increases when the noise added to the  
 570 modeled radar signal increases. This increase is approximately 1 Vol.% when the noise on the  
 571 radar signal increases from  $\pm 0.75$  dB to  $\pm 1.00$  dB (Table 9). Finally, Table 9 also shows that the  
 572 three inversion configurations provide un-biased  $M_v$  estimates and significant correlation  
 573 coefficient ( $R^2$  between 0.77 and 0.90).

574 **Table 9.** Statistical indexes on  $M_v$  estimates according to the three inversion configurations  
 575 (RMSE (Vol.%) | RRMSE (%) | MAPE (%) | bias (Vol.%) |  $R^2$ ). Configuration 1 uses HH and  
 576 NDVI, configuration 2 uses HV and NDVI, and configuration 3 uses HH, HV and NDVI.  
 577 Relative noise of the NDVI=15%.

	Noise on $\sigma_{tot}^0$ : $\pm 0.75$ dB	Noise on $\sigma_{tot}^0$ : $\pm 1.00$ dB
<b>Configuration 1 (HH and NDVI)</b>	4.5 16.5 17.1 0.0 0.85	5.5 19.8 21.0 0.0 0.78
<b>Configuration 2 (HV and NDVI)</b>	5.1 18.5 19.2 0.0 0.81	5.7 20.7 21.8 0.0 0.77
<b>Configuration 3 (HH, HV and NDVI)</b>	3.7 13.6 13.7 0.0 0.90	4.5 16.2 16.7 0.0 0.85

578 Figure 6 illustrates the RMSE evolution of  $M_v$  estimates as a function of NDVI for values  
 579 between 0.45 and 0.90 for each inversion configuration. For each value of NDVI, statistics were  
 580 calculated using all  $M_v$  values. The results showed that the RMSE of  $M_v$  estimates increases with  
 581 NDVI for all inversion configurations. As an example, in configuration 3 (HH, HV and NDVI),

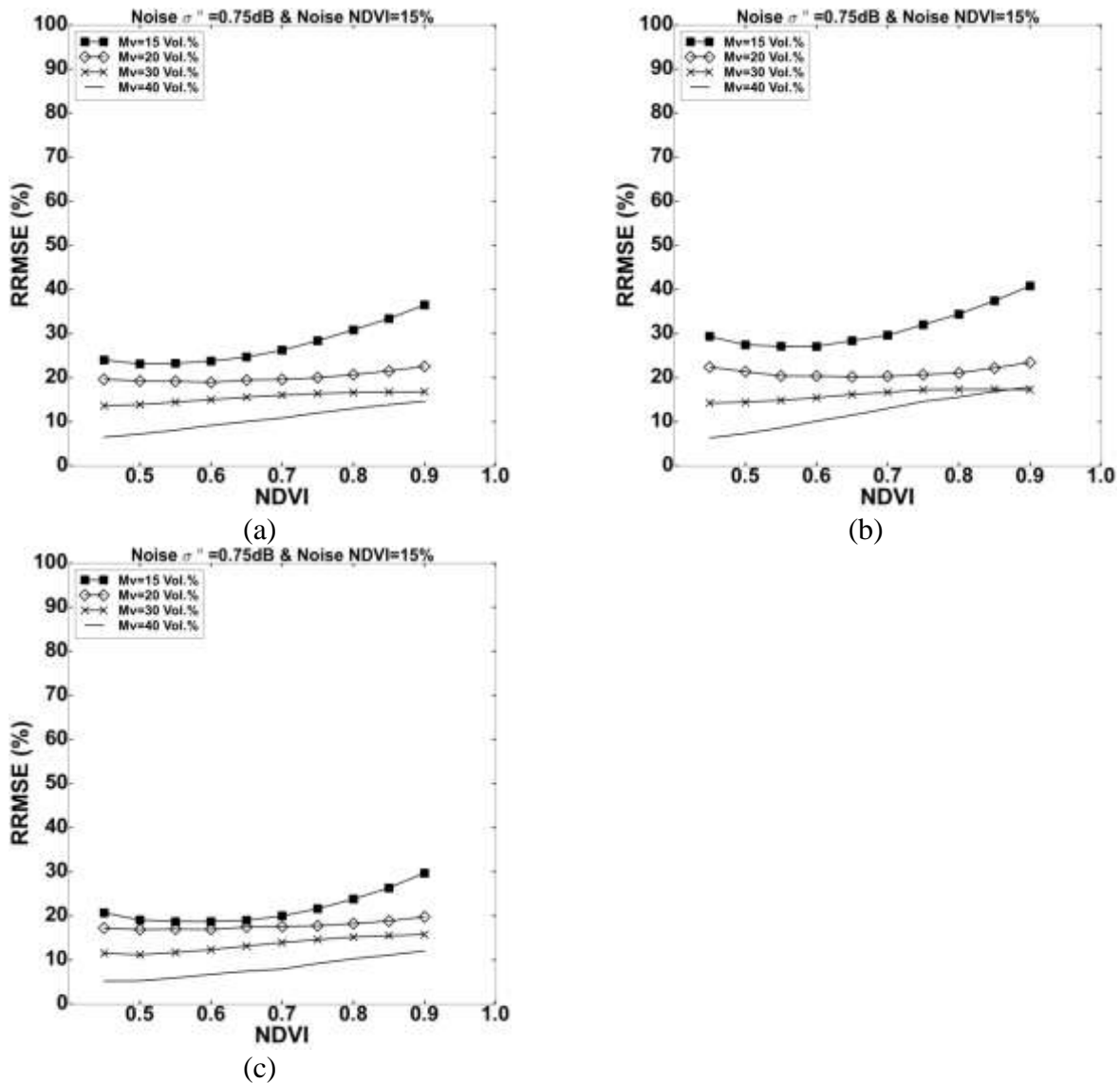
582 the RMSE of soil moisture estimates increases from 3.0 Vol.% for NDVI of 0.45 to 4.8 Vol.%  
 583 for a NDVI of 0.9 for a noise condition on the radar signal of  $\pm 0.75$  dB (Figure 6a). The results  
 584 showed that for a given NDVI value between 0.45 and 0.90, the RMSE is in same order in  
 585 configurations 1 and 2 (configuration 1 is slightly better than configuration 2) (Figure 6). In  
 586 addition, results obtained with HH were worse than those obtained with HH and HV.



587 **Figure 6.** Evolution of RMSE of  $M_v$  estimates according to the three inversion configurations as  
 588 a function of NDVI for noise conditions on the modeled radar signal of  $\pm 0.75$  dB (a), and  $\pm 1$  dB  
 589 (b).

590 Moreover, the performances of neural networks for estimating soil moisture were analyzed  
 591 according to NDVI for given  $M_v$  values (Figure 7). The results showed that the relative RMSE  
 592 ( $RRMSE = RMSE / M_v$ ) of  $M_v$  estimates increases with the NDVI for the three inversion  
 593 configurations. Indeed, as the vegetation grows (i.e., increasing NDVI values) the soil  
 594 contribution decreases and the backscattering coefficients become less sensitive to soil moisture.

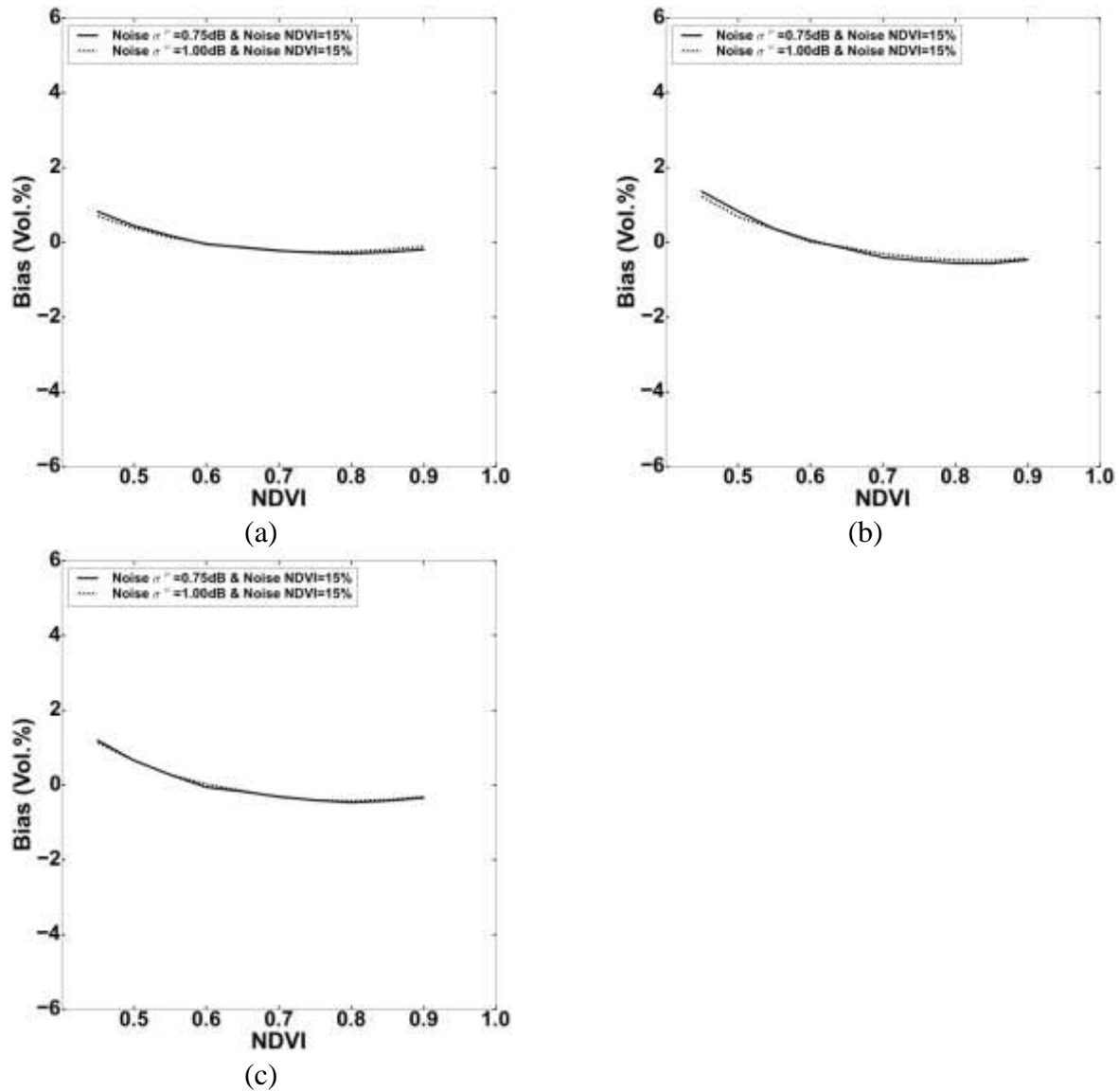
595 In addition, for a given NDVI between 0.45 and 0.90 the RRMSE decreases when  $M_v$  increases  
596 (Figure 7) because for a given NDVI value the soil contribution is more important for high than  
597 for low soil moisture conditions, and consequently, the errors on  $M_v$  estimates decrease when  $M_v$   
598 increases. As an example, in configuration 1 (HH and NDVI), for a NDVI of 0.75 (LAI about 3  
599  $\text{m}^2/\text{m}^2$ ), the RRMSE values are approximately 28.3, 20.0, 16.3, and 12.0% for reference  $M_v$  of  
600 15, 20, 30 and 40 Vol.%, respectively. For low  $M_v$  (lower than 20 Vol.%), the RRMSE increases  
601 significantly with NDVI for high NDVI values (higher than 0.75, LAI about 3  $\text{m}^2/\text{m}^2$ ) in  
602 comparison to the RRMSE observed for higher  $M_v$  values (higher than 20 Vol.%). As an  
603 example, in configuration 3 (HH, HV and NDVI), the RRMSE on  $M_v$  estimates increases for  $M_v$   
604 of 15 Vol.% and noise condition on the simulated radar signal of 0.75 dB from approximately  
605 21% for NDVI=0.45 to 30% for NDVI=0.90. This increase in the RRMSE is only approximately  
606 5% for  $M_v$  of 30 Vol.% (RRMSE increases from approximately 11% for NDVI=0.45 to 16% for  
607 NDVI=0.90) (Figure 7).



608 **Figure 7.** Evolution of the relative RMSE (in percent) of  $M_v$  estimates ( $RRMSE=RMSE/ M_v$ )  
 609 according to NDVI and  $M_v$ . (a) configuration 1: HH and NDVI, (b) configuration 2: HV and  
 610 NDVI, and (c) configuration 3: HH, HV and NDVI.

611 The difference between the estimated and reference  $M_v$  were also analyzed as a function of  
 612 NDVI using for each NDVI and all  $M_v$  values (Figure 8). For a given NDVI between 0.45 and  
 613 0.90, the bias on  $M_v$  estimates is similar for radar signal noise of  $\pm 0.75$  and  $\pm 1$  dB. The results  
 614 showed a slight underestimation (lower than approximately 1 Vol.%) of  $M_v$  estimates for NDVI

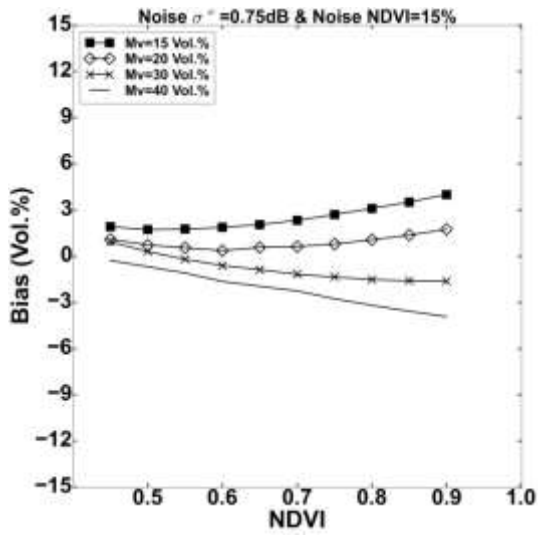
615 values between 0.60 (LAI about  $1\text{ m}^2/\text{m}^2$ ) and 0.90 (LAI about  $6\text{ m}^2/\text{m}^2$ ). In addition, a slight  
 616 overestimation of  $M_v$  is observed for a NDVI lower than 0.60 (lower than approximately 1 Vol.  
 617 %).



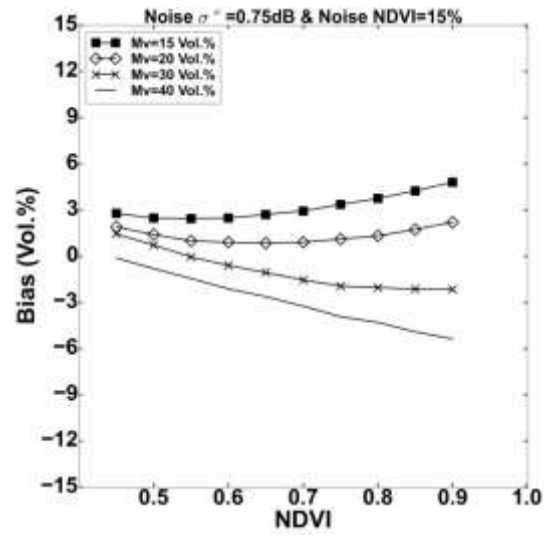
618 **Figure 8.** Evolution of the bias (estimated  $M_v$  – reference  $M_v$ ) of  $M_v$  estimates according to  
 619 NDVI values. (a) Inversion configuration 1, (b) inversion configuration 2, and (c) inversion  
 620 configuration 3.

621 Figure 9 shows the evolution of bias on  $M_v$  estimates obtained for the three inversion  
622 configurations as a function of the NDVI for some  $M_v$  values (15, 20, 30 and 40 Vol.%). For  
623 NDVI values lower than approximately 0.65 (LAI about  $1.5 \text{ m}^2/\text{m}^2$ ), the bias on  $M_v$  estimates is  
624 lower than 1.5 Vol.% for  $M_v$  between 15 and 40 Vol.%, in the case of configurations 1 and 3. For  
625 the inversion configuration 2, the bias reaches 5.4 Vol.% (for  $M_v= 40 \text{ Vol.}\%$ ). In addition, results  
626 showed that the bias increased when the NDVI increased, regardless of the  $M_v$  values. This  
627 increase was mainly observed when the NDVI was greater than 0.75 (LAI about  $3 \text{ m}^2/\text{m}^2$ ) for  
628 low  $M_v$  values (Figure 9). An overestimation of  $M_v$  estimates is mainly observed for  $M_v$  values  
629 lower than 20 Vol.%, while an underestimation is mainly observed for  $M_v$  values higher than 30  
630 Vol.%. Figure 9 also showed that for a given  $M_v$ , the bias is lower for configurations 1 and 3.  
631 The bias reaches 3.5 Vol.% for configurations 1 and 3 compared to 5 Vol.% for configuration 2  
632 for NDVI = 0.9 and  $M_v = 15 \text{ Vol.}\%$ . Figure 10 shows an example of box plots calculated for the  
633 inversion of configuration 3 and some NDVI values (0.6, 0.7, 0.8 and 0.9).

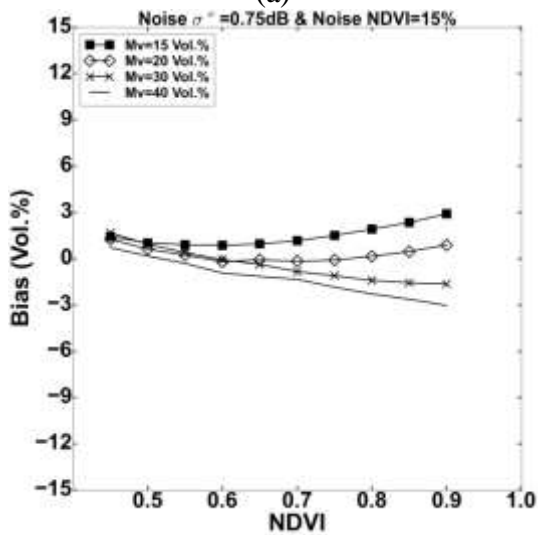
634



(a)

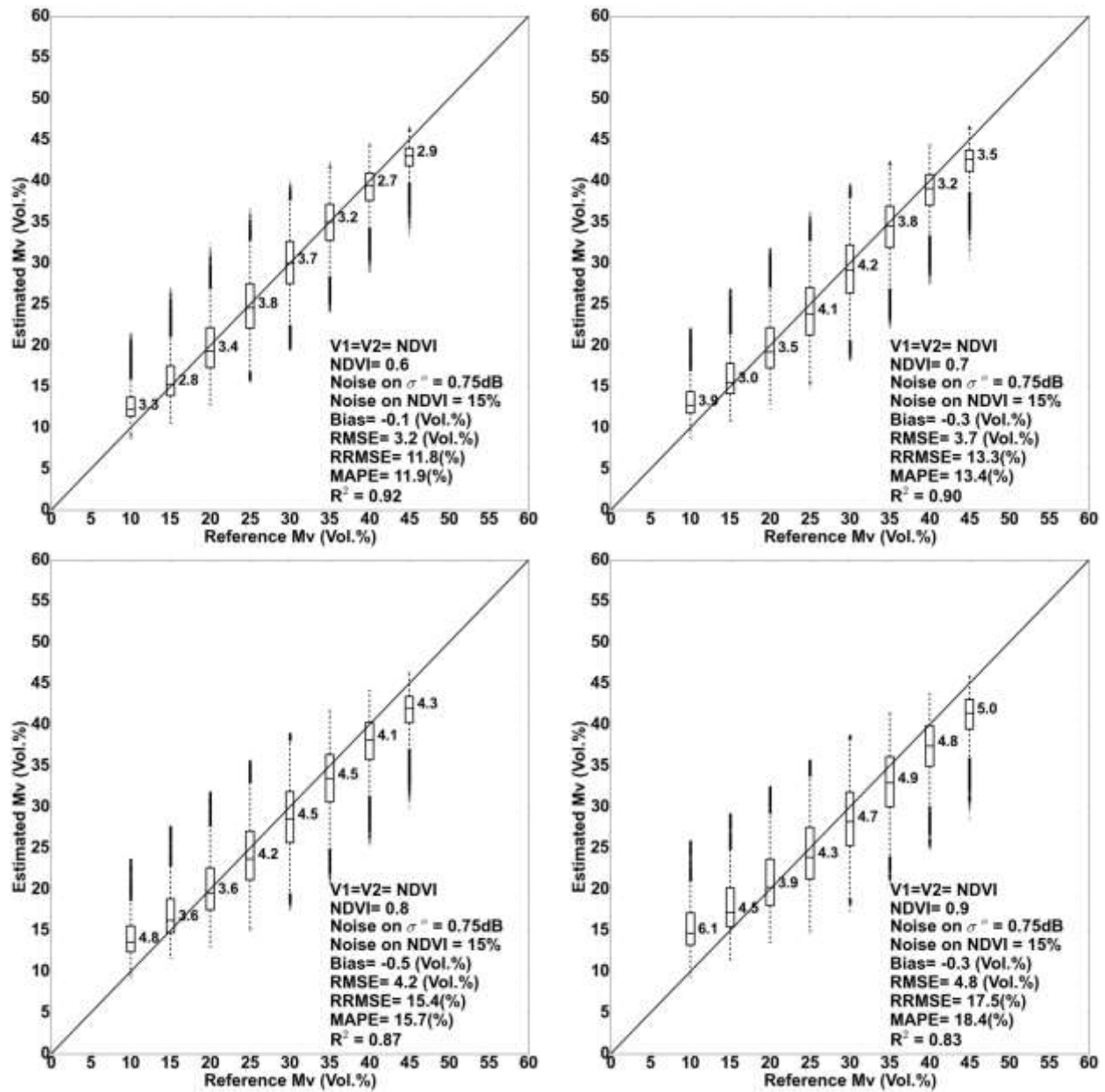


(b)



(c)

635 **Figure 9.** Evolution of the **bias** (estimated  $M_v$  – reference  $M_v$ ) on  $M_v$  estimates according to  
 636 NDVI and  $M_v$  values for noise on the modeled radar signal of 0.75 dB. (a) configuration 1, (b)  
 637 configuration 2, and (c) configuration 3.



638 **Figure 10.** Box plots of  $M_v$  estimates retrieved from the synthetic dataset. Neural networks were  
 639 trained and validated according to configuration 3 (using HH, HV and NDVI). Noise on the  
 640 modeled radar signal is  $\pm 0.75$  dB, and noise on NDVI is 15% of the NDVI value. Values to the  
 641 right of the box plots represent the RMSE on  $M_v$  estimates for a given reference  $M_v$ .

642 Moreover, 5-fold cross-validation was used to predict errors on  $M_v$  estimates for each  
643 inversion configuration performed using the synthetic dataset with LAI, FAPAR, and FCOVER  
644 as vegetation descriptors. Table 10 shows statistics (RMSE, RRMSE, MAPE, bias, and  $R^2$ ) on  
645  $M_v$  estimates computed from the validation dataset for reference  $M_v$  values between 10 and 45  
646 Vol.% and a LAI between 0 and 6 and FAPAR (as well as FCOVER) between 0 and 1. The results  
647 show that regardless of the vegetation descriptor used, the RMSE on  $M_v$  estimates is lower using  
648 HH compared to HV polarization (configuration 1 in comparison to configuration 2). In addition,  
649 the use of HH and HV polarizations slightly decreases the RMSE on  $M_v$  estimates. Table 10 also  
650 shows that the RMSE on  $M_v$  estimates increases approximately 1 Vol.% when noise added to the  
651 radar signal increases. For each inversion configuration and for a given noise condition on the  
652 modeled radar signal, the RMSE on  $M_v$  estimates is in the same order with the use of NDVI,  
653 LAI, FAPAR, or FCOVER as a vegetation descriptor (Table 10). Finally, the results showed that  
654 whatever the vegetation descriptor used, the three inversion configurations provide un-biased  $M_v$   
655 estimates.

656 **Table 10.** RMSE and Bias on  $M_v$  estimates according to the three inversion configurations  
 657 (RMSE (Vol.%) | RRMSE (%) | MAPE (%) | bias (Vol.%) |  $R^2$ ). Configuration 1 uses HH and  
 658 vegetation descriptor, configuration 2 uses HV and vegetation descriptor, and configuration 3  
 659 uses HH, HV and vegetation descriptor.

	Noise on $\sigma_{tot}^0$ : $\pm 0.75$ dB	Noise on $\sigma_{tot}^0$ : $\pm 1.00$ dB
V1=V2=NDVI Relative noise = 15 %		
Configuration 1	4.5 16.5 17.1 0.0 0.85	5.5 19.8 21.0 0.0 0.78
Configuration 2	5.1 18.5 19.2 0.0 0.81	5.7 20.7 21.8 0.0 0.77
Configuration 3	3.7 13.6 13.7 0.0 0.90	4.5 16.2 16.7 0.0 0.85
V1=V2=LAI Relative noise = 30 %		
Configuration 1	5.6 20.5 20.6 0.0 0.76	6.7 24.5 25.4 0.0 0.65
Configuration 2	7.1 26.0 26.9 0.0 0.61	8.1 29.3 31.2 0.0 0.50
Configuration 3	5.2 0.0 18.9 18.8 0.79	5.8 21.1 21.3 0.0 0.74
V1=V2=FAPAR Relative noise = 20 %		
Configuration 1	5.2 18.9 18.8 0.0 0.79	6.4 23.1 24.1 0.0 0.69
Configuration 2	6.3 22.8 23.3 0.0 0.70	7.3 26.7 28.0 0.0 0.59
Configuration 3	4.4 16.0 15.7 0.0 0.85	5.4 19.7 19.9 0.0 0.78
V1=V2=FCOVER Relative noise = 20 %		
Configuration 1	5.2 18.7 18.8 0.0 0.80	6.5 23.8 24.4 0.0 0.67
Configuration 2	7.1 25.7 26.7 0.0 0.62	7.8 28.3 30.0 0.0 0.54
Configuration 3	4.7 16.9 16.8 0.0 0.84	5.7 20.7 20.9 0.0 0.75

660 4.2.2 Real dataset

661 The capacity of the developed Neural Networks (NNs) to correctly estimate the soil moisture  
662 was then tested using the real dataset. The NNs applied to the real validation dataset are those  
663 which have been trained and validated using the synthetic dataset. NDVI, LAI, FAPAR and  
664 FCOVER derived from optical images were used as the input vegetation descriptors for the  
665 trained NNs. Inversion results obtained with the NDVI derived from optical images as the  
666 vegetation descriptor will be provided in detail, whereas the results based on the LAI, FAPAR,  
667 FCOVER derived from optical images as the vegetation descriptor will be briefly described.

668 First, statistics (RMSE, RRMSE, MAPE, bias,  $R^2$ ) on  $M_v$  estimates were also computed for  
669 all NDVI observations (Table 11). Slightly better statistics were observed with the noise on a  
670 modeled radar signal of  $\pm 1.00$  dB. With the noise of  $\pm 1.00$  dB, the RMSE is 4.5, 6.0 and 5.5  
671 Vol.% in configuration 1, 2 and 3, respectively. Moreover, a slight underestimation (about -0.1  
672 Vol.%) was observed in configuration 1 for the noise conditions of  $\pm 0.75$  dB and  $\pm 1.00$  dB. For  
673 configurations 2 and 3, an underestimation of  $M_v$  estimates was observed (about -1.4 Vol.% in  
674 configuration 2 and -1 Vol.% in configuration 3).

675 **Table 11.** statics on  $M_v$  estimates according to the three inversion configurations (RMSE  
676 (Vol.%) | RRMSE (%) | MAPE (%) | bias Vol.% |  $R^2$  | samples). Configuration 1 uses HH and  
677 NDVI, configuration 2 uses HV and NDVI, and configuration 3 uses HH, HV and NDVI.  
678 Relative noise on the NDVI=15%. Real SAR measurements and the LAI derived from optical  
679 images were used to estimate  $M_v$ .

	Noise on $\sigma_{tot}^0 : \pm 0.75$ dB	Noise on $\sigma_{tot}^0 : \pm 1.00$ dB
	NDVI = [0.45-0.90]	NDVI = [0.45-0.90]
<b>Configuration 1 (HH and NDVI)</b>	4.9 18.4 16.4 -0.1 0.60 93	4.5 17.0 15.5 -0.1 0.63 93
<b>Configuration 2 (HV and NDVI)</b>	6.8 25.7 23.1 -1.3 0.37 93	6.0 22.6 19.8 -1.3 0.42 93
<b>Configuration 3 (HH, HV and NDVI)</b>	6.2 23.5 21.2 -0.8 0.49 93	5.5 20.5 18.0 -0.9 0.53 93

680 Next, the statistics were computed from the real dataset of validation for NDVI classes of 0.05  
681 (NDVI was derived from optical images are between 0.45 and 0.9). The results showed that the  
682 RMSE on  $M_v$  estimates was in the same order for NDVI classes between 0.45 and 0.75 (LAI  
683 about  $3\text{m}^2/\text{m}^2$ ) on the one hand (difference lower than 1 Vol.%), and on the other hand for NDVI  
684 classes between 0.75 (LAI about  $3\text{m}^2/\text{m}^2$ ) and 0.90 (LAI about  $6\text{m}^2/\text{m}^2$ ). Therefore, the results  
685 of  $M_v$  estimates were presented for two classes of NDVI: NDVI lower and higher than 0.75  
686 (Table 12). The comparison between estimated  $M_v$  and  $M_v$  ground-truthed measurements is  
687 given in Figures 11 and 12. RMSE and bias on  $M_v$  estimates are lower with the noise condition  
688 on the modeled radar signal of  $\pm 1$  dB.

689 RMSE of 3.6 (RRMSE and MAPE about 12%), 5.4 (RRMSE and MAPE about 18%), and 4.4  
690 (RRMSE and MAPE about 15%) Vol.% were observed for configurations 1, 2 and 3,  
691 respectively, in the case of a NDVI lower than 0.75 and for modeled radar signal noise of  $\pm 1$  dB

692 (Table 12, Figure 11). For a NDVI higher than 0.75, the RMSE on  $M_v$  estimates is 6.1 (RRMSE  
693 and MAPE about 24%), 7.1 (RRMSE and MAPE about 28%) and 7.3 (RRMSE and MAPE  
694 about 29%) Vol.%, respectively, for configurations 1, 2 and 3 and for the noise on the modeled  
695 radar signal of  $\pm 1$  dB (Table 12, Figure 11). Moreover, results showed that for a NDVI  $< 0.75$   
696 the trained NNs provide  $M_v$  estimates with slight bias (0.2, -1.7, and -0.9 Vol.% in  
697 configurations 1, 2 and 3, respectively) (Table 12, Figure 11). For a NDVI  $> 0.75$ , an slight bias  
698 (between -1 and 0.1 Vol.%) was observed for the noise on the radar signal of  $\pm 1$  dB, with the  
699 lower value for the inversion using HH and NDVI (0.1 Vol.%) (Table 12, Figure 11).

700 **Table 12.** RMSE and bias on  $M_v$  estimates according to the three inversion configurations  
701 (RMSE (Vol.%) | RRMSE (%) | MAPE (%) | bias Vol.% |  $R^2$  | samples). Configuration 1 uses  
702 HH and NDVI, configuration 2 uses HV and NDVI, and configuration 3 uses HH, HV and  
703 NDVI. Relative noise on the NDVI=15%. Real SAR measurements and NDVI derived from  
704 optical images were used to estimate  $M_v$ .

	Noise on $\sigma_{tot}^0 : \pm 0.75$ dB		Noise on $\sigma_{tot}^0 : \pm 1.00$ dB	
	NDVI $< 0.75$	NDVI $> 0.75$	NDVI $< 0.75$	NDVI $> 0.75$
<b>Configuration 1</b>	3.8 13.9 12.4  0.0 0.77 64	6.6 27.3 25.3  -0.3 0.07 29	3.6 13.1 11.8  -0.2 0.79 64	6.1 24.9 23.5  0.1 0.10 29
<b>Configuration 2</b>	6.0 21.7 19.8  -1.5 0.52 64	8.4 34.5 30.6  -0.8 0.04 29	5.4 19.7 17.0  -1.7 0.56 64	7.1 29.2 26.1  -0.5 0.07 29
<b>Configuration 3</b>	5.0 18.2 16.8  -0.7 0.67 64	8.3 34.2 30.9  -1.1 0.04 29	4.4 15.8 13.9  -0.9 0.71 64	7.3 30.1 26.9  -1.0 0.06 29

705 Moreover, the SAR real validation dataset was inverted to estimate soil moisture by means of  
706 trained NNs with the use of each of the vegetation descriptors derived from optical images LAI,

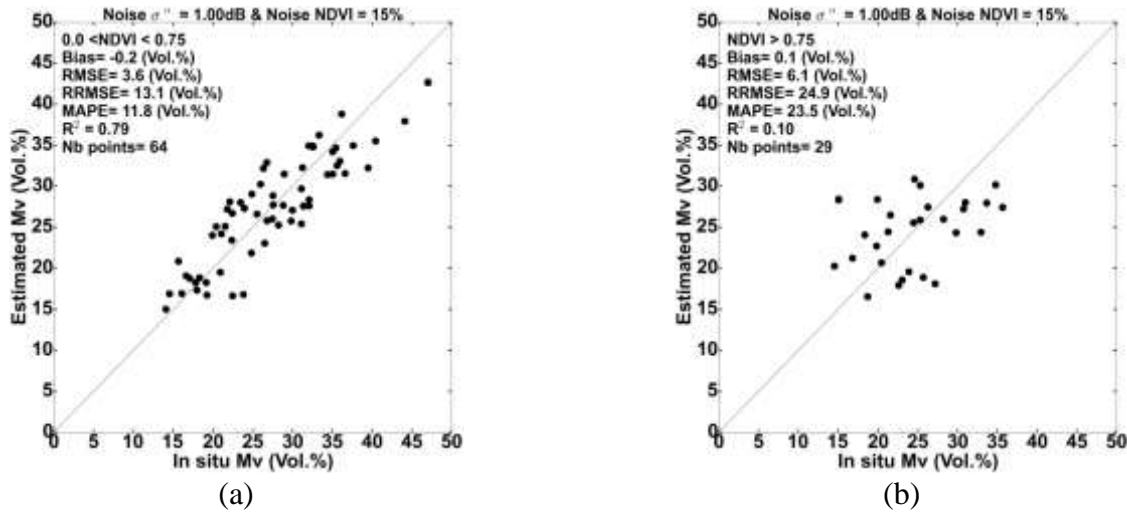
707 FAPAR, and FCOVER). Table 13 shows the (RMSE, RRMSE, MAPE, bias,  $R^2$ ) on  $M_v$   
708 estimates in the three inversion configurations for two classes of NDVI: NDVI lower and higher  
709 than 0.75 (LAI about  $3\text{m}^2/\text{m}^2$ ). The results showed that the RMSE (as well as RRMSE, MAPE)  
710 on  $M_v$  estimates are almost similar, regardless of which vegetation descriptors derived from  
711 optical images were used (NDVI, LAI, FAPAR, or FCOVER) (Table 13).

712 In conclusion, the use of HH polarization in addition to a vegetation descriptor derived from  
713 optical images (Configuration 1) provides a better estimation of the soil moisture with a RMSE  
714 approximately 4.5 and 7.0 Vol.% for a NDVI lower and higher than 0.75 (LAI about  $3\text{m}^2/\text{m}^2$ ),  
715 respectively. The use of HV in addition to HH slightly lowers the precision of  $M_v$  estimates.

716

717 **Table 13.** Statics on  $M_v$  estimates according to the three inversion configurations (RMSE  
718 (Vol.%) | RRMSE (%) | MAPE (%) | bias Vol.% |  $R^2$  | samples). Configuration 1 uses HH and  
719 NDVI, configuration 2 uses HV and NDVI, and configuration 3 uses HH, HV and NDVI. Real  
720 SAR measurements, and NDVI, LAI, FAPAR and FCOVER derived from optical images were  
721 used to estimate  $M_v$ .

	Noise on $\sigma_{tot}^0 : \pm 0.75$ dB		Noise on $\sigma_{tot}^0 : \pm 1.00$ dB	
	NDVI < 0.75	NDVI > 0.75	NDVI < 0.75	NDVI > 0.75
<b>V1=V2=NDVI</b>				
Relative noise = 15 %				
Configuration 1	3.8 13.9 12.4  0.0 0.77 64	6.6 27.3 25.3  -0.3 0.07 29	3.6 13.1 11.8  -0.2 0.79 64	6.1 24.9 23.5  0.1 0.10 29
Configuration 2	6.0 21.7 19.8  -1.5 0.52 64	8.4 34.5 30.6  -0.8 0.04 29	5.4 19.7 17.0  -1.7 0.56 64	7.1 29.2 26.1  -0.5 0.07 29
Configuration 3	5.0 18.2 16.8  -0.7 0.67 64	8.3 34.2 30.9  -1.1 0.04 29	4.4 15.8 13.9  -0.9 0.71 64	7.3 30.1 26.9  -1.0 0.06 29
<b>V1=V2=LAI</b>				
Relative noise = 30 %				
Configuration 1	4.7 17.1 15.9  -0.0 0.65 64	7.3 29.7 27.2  -1.5 0.02 29	4.5 16.3 15.3  0.6 0.67 64	7.5 30.6 28.9  0.3 0.00 29
Configuration 2	7.5 27.1 23.8  -1.1 0.36 64	10.0 41.0 34.9  -3.2 0.00 29	7.1 25.8 22.2  -1.1 0.35 64	9.0 36.8 31.4  -2.5 0.00 29
Configuration 3	5.6 20.1 17.3  -0.9 0.57 64	8.4 34.5 30.5  -2.5 0.00 29	5.7 20.7 17.7  -0.5 0.55 64	8.7 35.7 31.1  -2.2 0.00 29
<b>V1=V2=FAPAR</b>				
Relative noise = 20 %				
Configuration 1	5.0 18.1 16.2  0.5 0.63 64	7.9 32.6 30.3  -0.7 0.00 29	4.9 17.8 16.6  1.2 0.63 64	7.4 30.4 29.0  0.7 0.00 29
Configuration 2	8.1 29.2 25.8  -0.0 0.34 64	10.9 44.6 39.3  -3.1 0.00 29	7.2 26.2 22.4  -0.1 0.34 64	9.1 37.2 32.5  -1.7 0.00 29
Configuration 3	6.4 23.3 20.5  0.4 0.52 64	9.5 38.9 34.2  -2.4 0.00 29	6.2 22.4 19.5  0.9 0.51 64	8.8 36.1 32.4  -1.3 0.01 29
<b>V1=V2=FCOVER</b>				
Relative noise = 20 %				
Configuration 1	5.1 18.6 16.5  0.8 0.62 64	8.0 33.0 30.7  -0.7 0.01 29	5.0 18.3 17.1  0.9 0.62 64	6.8 27.5 25.2  -0.4 0.03 29
Configuration 2	7.6 27.5 23.7  -0.6 0.34 64	10.0 40.9 35.1  -3.3 0.01 29	7.2 25.9 21.8  -0.7 0.34 64	9.1 37.2 31.9  -2.5 0.01 29
Configuration 3	6.0 21.6 19.0  0.3 0.55 64	9.2 37.6 32.7  -2.5 0.01 29	5.9 21.4 18.2  0.2 0.54 64	8.4 34.5 30.1  -1.9 0.01 29



723 **Figure 11.** Retrieved soil moisture using configuration 1 versus ground-truthed measurements  
 724 for NDVI lower and higher than 0.75 (a, and b respectively). Noise on radar signal =  $\pm 1$ dB. Bias  
 725 = estimated  $M_v$  - reference  $M_v$ .  
 726

727 **5. Conclusion**

728 Inversion results of the synthetic dataset showed that the best  $M_v$  estimates were obtained  
 729 with the use of the X-band radar signal in HH polarization or in using both HH and HV  
 730 polarizations, in addition to one vegetation descriptor derived from optical images. However, the  
 731 use of HV in addition to one vegetation descriptor derived from optical images degrades the  
 732 precision on  $M_v$  estimates. Moreover, results showed that the RMSE on  $M_v$  estimates is slightly  
 733 sensitive to additive noise on the modelled radar signal. The RMSE increases approximately 1  
 734 Vol.% when the noise of the radar signal increases from  $\pm 0.75$  dB to  $\pm 1.00$  dB. For all NDVI  
 735 values, the RMSE on  $M_v$  estimates ( $M_v$  between 10 and 45 Vol.%) was approximately 5.0 Vol.%  
 736 (RRMSE and MAPE about 19 %) in configurations 1 and 3. Similar values of the RMSE (as well  
 737 as RRMSE and MAPE) on  $M_v$  estimates were obtained with the use of LAI, FAPAR, and  
 738 FCOVER as the vegetation descriptor. The accuracy of  $M_v$  estimates degrades (i.e., an increase  
 739 in the RMSE, RRMSE, and MAPE) with vegetation growth (i.e., an increase in the NDVI). As  
 740 an example, in configuration 3 (HH, HV and NDVI), the RMSE on  $M_v$  estimates increases from

741 3.6 Vol.% (RRMSE about 13%) for NDVI of 0.45 to 5.7 Vol.% (RRMSE about 21 %) for a  
742 NDVI of 0.9.

743 From the real validation dataset (53% of the real dataset), the soil moisture estimation using  
744 the X-band SAR data in addition to one vegetation descriptor derived from optical images allows  
745 better results with HH polarization than with HV or both HH and HV. With HH and NDVI  
746 information derived from optical images, the accuracy on the soil moisture estimation was 3.6  
747 Vol.% (RRMSE and MAPE about 13%) for NDVI between 0 and 0.75 (LAI about 3 m<sup>2</sup>/m<sup>2</sup>) and  
748 6.1 Vol.% (RRMSE and MAPE about 25%) when the NDVI of the grassland was between 0.75  
749 and 0.9 (LAI about 6 m<sup>2</sup>/m<sup>2</sup>). Similar results were obtained regardless the vegetation descriptor  
750 used.

751 With the arrival of new satellites, such as SENTINEL-1A (launched on 3 April 2014), in  
752 addition to future satellites SENTINEL-1B, SENTINEL-2A (optical sensor), and SENTINEL-  
753 2B, it will be possible to obtain SAR (C-band) and optical remote sensing data covering global  
754 areas with high spatial and temporal resolutions (2 days with 2 SENTINEL-1 satellites, and 5  
755 days for 2 SENTINEL-2 satellites at 10 m spatial resolution). Combining SENTINEL-1 data  
756 with optical images (SENTINEL-2, LANDSAT-7/8) will allow more precise estimation of  $M_v$   
757 because the radar signal penetration depth into vegetation cover is higher in the C-band  
758 compared to the X-band. This work is in the context of preparing for SENTINEL 1 and 2  
759 missions.

760 This study demonstrated that the use of NNs technique to invert X-band SAR backscattering  
761 coefficients allows the estimation of soil moisture with acceptable accuracy (RMSE of 3.6 Vol.%  
762 for a NDVI lower than 0.75). Current remote sensing sensors (optical and SAR) and those  
763 available in the near future (spatial resolution better than 10 m) will allow the estimation of soil

764 moisture at a field scale with high temporal resolution (better than weekly). Vegetation  
765 biophysical parameters (i.e., LAI) and soil moisture that can be derived from optical and SAR  
766 images could be useful to calibrate crop models for better irrigation management and crop  
767 growth monitoring. Indeed, combining optical and SAR data would enhance the relevance of  
768 remote sensing data for water and crop monitoring.

769 **Acknowledgements**

770 This research was supported by the French Space Study Center (CNES, DAR 2014 TOSCA)  
771 and the Islamic Development Bank (PhD Scholarship of M. Mohammad El Hajj). Field  
772 experiments were carried out within the SicMed-Crau program. The CSK images used in this  
773 analysis were supported by public funds received in the GEOSUD framework, a project (ANR-  
774 10-EQPX-20) of the "Investissements d'Avenir" program managed by the French National  
775 Research Agency. The authors wish to thank the German Space Agency (DLR) for kindly  
776 providing the TSX images under proposal HYD0007. We also wish to thank the EMMAH unit  
777 (INRA) for providing meteorological data and the technical teams of ASI and DLR for providing  
778 answers regarding the performances of CSK and TSX. Finally, we would like to thank Olivier  
779 Hagolle (CNES-CESBIO: Centre National d'Etudes Spatiales-Centre d'Etudes Spatiales de la  
780 BIOSphère) for providing calibrated SPOT 4 images in the framework of Take 5 experiments.

781

782 **References**

- 783 Agapiou, A., Hadjimitsis, D.G., Papoutsas, C., Alexakis, D.D., and Papadavid, G. (2011). The  
784 importance of accounting for atmospheric effects in the application of NDVI and interpretation  
785 of satellite imagery supporting archaeological research: the case studies of Palaepaphos and Nea  
786 Paphos sites in Cyprus. *Remote Sens.* *3*, 2605–2629.
- 787 Agenzia Spaziale Italiana (2007). COSMO-SkyMed System Description & User Guide.
- 788 Allen, R.G., Pereira, L.S., Raes, D., and Smith, M. (1998). Crop evapotranspiration-Guidelines  
789 for computing crop water requirements-FAO Irrigation and drainage paper 56. FAO Rome *300*,  
790 6541.
- 791 Attema, E.P.W., and Ulaby, F.T. (1978). Vegetation modeled as a water cloud. *Radio Sci.* *13*,  
792 357–364.
- 793 Aubert, M., Baghdadi, N., Zribi, M., Douaoui, A., Loumagne, C., Baup, F., El Hajj, M., and  
794 Garrigues, S. (2011). Analysis of TerraSAR-X data sensitivity to bare soil moisture, roughness,  
795 composition and soil crust. *Remote Sens. Environ.* *115*, 1801–1810.
- 796 Baghdadi, N., Cresson, R., El Hajj, M., Ludwig, R., and La Jeunesse, I. (2012). Estimation of  
797 soil parameters over bare agriculture areas from C-band polarimetric SAR data using neural  
798 networks. *Hydrol. Earth Syst. Sci.* *16*, 1607–1621.
- 799 Balenzano, A., Mattia, F., Satalino, G., and Davidson, M. (2011). Dense temporal series of C-  
800 and L-band SAR data for soil moisture retrieval over agricultural crops. *Sel. Top. Appl. Earth*  
801 *Obs. Remote Sens. IEEE J. Of* *4*, 439–450.
- 802 Baret, F., and Guerif, M. (2006). Remote detection and quantification of plant stress:  
803 opportunities remote sensing observations. In *Comparative Biochemistry and Physiology a-  
804 Molecular & Integrative Physiology*, (ELSEVIER SCIENCE INC 360 PARK AVE SOUTH,  
805 NEW YORK, NY 10010-1710 USA), pp. S148–S148.
- 806 Baret, F., and Guyot, G. (1991). Potentials and limits of vegetation indices for LAI and APAR  
807 assessment. *Remote Sens. Environ.* *35*, 161–173.
- 808 Baret, F., Hagolle, O., Geiger, B., Bicheron, P., Miras, B., Huc, M., Berthelot, B., Niño, F.,  
809 Weiss, M., and Samain, O. (2007). LAI, fAPAR and fCover CYCLOPES global products  
810 derived from VEGETATION: Part 1: Principles of the algorithm. *Remote Sens. Environ.* *110*,  
811 275–286.
- 812 Botha, E.J., Leblon, B., Zebarth, B.J., and Watmough, J. (2010). Non-destructive estimation of  
813 wheat leaf chlorophyll content from hyperspectral measurements through analytical model  
814 inversion. *Int. J. Remote Sens.* *31*, 1679–1697.
- 815 Bottraud, J.C., Bornand, M., and Servat, E. (1984). Mesures de résistivité appliquées à la  
816 cartographie en pédologie. *Sci. Sol* *4*, 279–294.

- 817 Brereton, A.J., and Hope-Cawdery, M. (1988). Drumlin soils: the depression of herbage yield by  
818 shallow water table depth. *Ir. J. Agric. Res.* 167–178.
- 819 Brown, S.C., Quegan, S., Morrison, K., Bennett, J.C., and Cookmartin, G. (2003). High-  
820 resolution measurements of scattering in wheat canopies-Implications for crop parameter  
821 retrieval. *Geosci. Remote Sens. IEEE Trans. On* 41, 1602–1610.
- 822 Bsaibes, A., Courault, D., Baret, F., Weiss, M., Olioso, A., Jacob, F., Hagolle, O., Marloie, O.,  
823 Bertrand, N., and Desfond, V. (2009). Albedo and LAI estimates from FORMOSAT-2 data for  
824 crop monitoring. *Remote Sens. Environ.* 113, 716–729.
- 825 Carlson, T.N., and Ripley, D.A. (1997). On the relation between NDVI, fractional vegetation  
826 cover, and leaf area index. *Remote Sens. Environ.* 62, 241–252.
- 827 Carlson, T.N., Gillies, R.R., and Perry, E.M. (1994). A method to make use of thermal infrared  
828 temperature and NDVI measurements to infer surface soil water content and fractional  
829 vegetation cover. *Remote Sens. Rev.* 9, 161–173.
- 830 Ceccato, P., Flasse, S., Tarantola, S., Jacquemoud, S., and Grégoire, J.-M. (2001). Detecting  
831 vegetation leaf water content using reflectance in the optical domain. *Remote Sens. Environ.* 77,  
832 22–33.
- 833 Chai, S.-S., Walker, J.P., Makarynsky, O., Kuhn, M., Veenendaal, B., and West, G. (2009). Use  
834 of soil moisture variability in artificial neural network retrieval of soil moisture. *Remote Sens.* 2,  
835 166–190.
- 836 Champion, I. (1991). Etude et mise au point de modèles Semi-empiriques représentant la réponse  
837 de couverts végétaux dans le domaine hyperfréquence. Complémentarité avec le domaine  
838 optique. Thèse, Université Paris VII. France.
- 839 Champion, I., and Guyot, G. (1991). Generalized formulation for semi-empirical radar models  
840 representing crop backscattering. *ESA Phys. Meas. Signal. Remote Sens.* 1, 269–272.
- 841 Claverie, M., Vermote, E.F., Weiss, M., Baret, F., Hagolle, O., and Demarez, V. (2013).  
842 Validation of coarse spatial resolution LAI and FAPAR time series over cropland in southwest  
843 France. *Remote Sens. Environ.* 139, 216–230.
- 844 Coletta, A., Angino, G., Battazza, F., Caltagirone, F., Impagnatiello, F., Valentini, G., Capuzi,  
845 A., Fagioli, S., and Leonardi, R. (2007). COSMO-SkyMed program: Utilization and description  
846 of an advanced space EO dual-use asset. In *Proc. Envisat Symp*, pp. 23–27.
- 847 Courault, D., Bsaibes, A., Kpemlie, E., Hadria, R., Hagolle, O., Marloie, O., Hanocq, J.-F.,  
848 Olioso, A., Bertrand, N., and Desfonds, V. (2008). Assessing the potentialities of FORMOSAT-2  
849 data for water and crop monitoring at small regional scale in South-Eastern France. *Sensors* 8,  
850 3460–3481.
- 851 Courault, D., Hadria, R., Ruget, F., Olioso, A., Duchemin, B., Hagolle, O., and Dedieu, G.  
852 (2010). Combined use of FORMOSAT-2 images with a crop model for biomass and water

853 monitoring of permanent grassland in Mediterranean region. *Hydrol. Earth Syst. Sci. Discuss.* 7,  
854 1731–1744.

855 Darvishzadeh, R., Skidmore, A., Schlerf, M., and Atzberger, C. (2008a). Inversion of a radiative  
856 transfer model for estimating vegetation LAI and chlorophyll in a heterogeneous grassland.  
857 *Remote Sens. Environ.* 112, 2592–2604.

858 Darvishzadeh, R., Skidmore, A., Atzberger, C., and van Wieren, S. (2008b). Estimation of  
859 vegetation LAI from hyperspectral reflectance data: Effects of soil type and plant architecture.  
860 *Int. J. Appl. Earth Obs. Geoinformation* 10, 358–373.

861 Del Frate, F., and Solimini, D. (2004). On neural network algorithms for retrieving forest  
862 biomass from SAR data. *Geosci. Remote Sens. IEEE Trans. On* 42, 24–34.

863 Del Frate, F., Ferrazzoli, P., and Schiavon, G. (2003). Retrieving soil moisture and agricultural  
864 variables by microwave radiometry using neural networks. *Remote Sens. Environ.* 84, 174–183.

865 De Roo, R.D., Du, Y., Ulaby, F.T., and Dobson, M.C. (2001). A semi-empirical backscattering  
866 model at L-band and C-band for a soybean canopy with soil moisture inversion. *Geosci. Remote*  
867 *Sens. IEEE Trans. On* 39, 864–872.

868 Dubois, P.C., Van Zyl, J., and Engman, T. (1995). Measuring soil moisture with imaging radars.  
869 *Geosci. Remote Sens. IEEE Trans. On* 33, 915–926.

870 Duveiller, G., Weiss, M., Baret, F., and Defourny, P. (2011). Retrieving wheat Green Area Index  
871 during the growing season from optical time series measurements based on neural network  
872 radiative transfer inversion. *Remote Sens. Environ.* 115, 887–896.

873 Eineder, M., Fritz, T., Mittermayer, J., Roth, A., Boerner, E., and Breit, H. (2008). TerraSAR-X  
874 Ground Segment, Basic Product Specification Document. (Munich, Germany: DTIC Document,  
875 Cluster Applied Remote Sensing. Available online: [https://tandemx-science.dlr.de/pdfs/TX-GS-DD-3302\\_Basic-Products-Specification-Document\\_V1.6.pdf](https://tandemx-science.dlr.de/pdfs/TX-GS-DD-3302_Basic-Products-Specification-Document_V1.6.pdf) (accessed on 22 April 2011).).

877 El Hajj, M., Bégué, A., Lafrance, B., Hagolle, O., Dedieu, G., and Rumeau, M. (2008). Relative  
878 radiometric normalization and atmospheric correction of a SPOT 5 time series. *Sensors* 8, 2774–  
879 2791.

880 Fensholt, R., Sandholt, I., and Rasmussen, M.S. (2004). Evaluation of MODIS LAI, fAPAR and  
881 the relation between fAPAR and NDVI in a semi-arid environment using in situ measurements.  
882 *Remote Sens. Environ.* 91, 490–507.

883 Fieuzal, R., Duchemin, B., Jarlan, L., Zribi, M., Baup, F., Merlin, O., Hagolle, O., and Garatuza-  
884 Payan, J. (2011). Combined use of optical and radar satellite data for the monitoring of irrigation  
885 and soil moisture of wheat crops. *Hydrol. Earth Syst. Sci.* 15, 1117–1129.

886 Fung, A.K., Li, Z., and Chen, K.S. (1992). Backscattering from a randomly rough dielectric  
887 surface. *Geosci. Remote Sens. IEEE Trans. On* 30, 356–369.

- 888 Gherboudj, I., Magagi, R., Berg, A.A., and Toth, B. (2011). Soil moisture retrieval over  
889 agricultural fields from multi-polarized and multi-angular RADARSAT-2 SAR data. *Remote*  
890 *Sens. Environ.* *115*, 33–43.
- 891 Guerschman, J.P., Hill, M.J., Renzullo, L.J., Barrett, D.J., Marks, A.S., and Botha, E.J. (2009).  
892 Estimating fractional cover of photosynthetic vegetation, non-photosynthetic vegetation and bare  
893 soil in the Australian tropical savanna region upscaling the EO-1 Hyperion and MODIS sensors.  
894 *Remote Sens. Environ.* *113*, 928–945.
- 895 Hagolle, O., Dedieu, G., Mougnot, B., Debaecker, V., Duchemin, B., and Meygret, A. (2008).  
896 Correction of aerosol effects on multi-temporal images acquired with constant viewing angles:  
897 Application to Formosat-2 images. *Remote Sens. Environ.* *112*, 1689–1701.
- 898 He, B., Xing, M., and Bai, X. (2014). A Synergistic Methodology for Soil Moisture Estimation  
899 in an Alpine Prairie Using Radar and Optical Satellite Data. *Remote Sens.* *6*, 10966–10985.
- 900 Hong, S., Malaterre, P.-O., Belaud, G., and Dejean, C. (2013). Optimization of water distribution  
901 for open-channel irrigation networks. *Press J. Hydroinformatics*.
- 902 Hosseini, M., and Saradjian, M.R. (2011). Soil moisture estimation based on integration of  
903 optical and SAR images. *Can. J. Remote Sens.* *37*, 112–121.
- 904 Iorio, M., Mecozzi, R., and Torre, A. (2010). Cosmo SkyMed: antenna elevation pattern data  
905 evaluation. *Ital. J Remote Sens* *42*, 69–77.
- 906 Leenhardt, D., Trouvat, J.-L., Gonzalès, G., Péronnaud, V., Prats, S., and Bergez, J.-E. (2004).  
907 Estimating irrigation demand for water management on a regional scale: I. ADEAUMIS, a  
908 simulation platform based on bio-decisional modelling and spatial information. *Agric. Water*  
909 *Manag.* *68*, 207–232.
- 910 Li, F., Chen, W., Zeng, Y., Zhao, Q., and Wu, B. (2014). Improving Estimates of Grassland  
911 Fractional Vegetation Cover Based on a Pixel Dichotomy Model: A Case Study in Inner  
912 Mongolia, China. *Remote Sens.* *6*, 4705–4722.
- 913 Marquardt, D.W. (1963). An algorithm for least-squares estimation of nonlinear parameters. *J.*  
914 *Soc. Ind. Appl. Math.* *11*, 431–441.
- 915 Masek, J.G., Vermote, E.F., Saleous, N., Wolfe, R., Hall, F.G., Huemmrich, F., Gao, F., Kutler,  
916 J., and Lim, T.K. (2013). LEDAPS calibration, reflectance, atmospheric correction preprocessing  
917 code, version 2. *Model Prod.*
- 918 Mattia, F., Le Toan, T., Picard, G., Posa, F.I., D’Alessio, A., Notarnicola, C., Gatti, A.M.,  
919 Rinaldi, M., Satalino, G., and Pasquariello, G. (2003). Multitemporal C-band radar  
920 measurements on wheat fields. *Geosci. Remote Sens. IEEE Trans. On* *41*, 1551–1560.
- 921 Mérot, A. (2007). Analyse et modélisation du fonctionnement biophysique et décisionnel d’un  
922 système prairial irrigué-Application aux prairies plurispécifiques de Crau en vue de l’élaboration

- 923 d'un Outil d'Aide à la Décision. Thèse, Ecole nationale supérieure agronomique de Montpellier-  
924 AGRO M. France.
- 925 Merot, A., Wery, J., Isberie, C., and Charron, F. (2008). Response of a plurispecific permanent  
926 grassland to border irrigation regulated by tensiometers. *Eur. J. Agron.* 28, 8–18.
- 927 North, P.R. (2002). Estimation of FAPAR, LAI, and vegetation fractional cover from ATSR-2  
928 imagery. *Remote Sens. Environ.* 80, 114–121.
- 929 Notarnicola, C., Angiulli, M., and Posa, F. (2006). Use of radar and optical remotely sensed data  
930 for soil moisture retrieval over vegetated areas. *Geosci. Remote Sens. IEEE Trans. On* 44, 925–  
931 935.
- 932 Oh, Y. (2004). Quantitative retrieval of soil moisture content and surface roughness from  
933 multipolarized radar observations of bare soil surfaces. *Geosci. Remote Sens. IEEE Trans. On*  
934 42, 596–601.
- 935 Paloscia, S., Pampaloni, P., Pettinato, S., and Santi, E. (2008). A comparison of algorithms for  
936 retrieving soil moisture from ENVISAT/ASAR images. *Geosci. Remote Sens. IEEE Trans. On*  
937 46, 3274–3284.
- 938 Paloscia, S., Pettinato, S., Santi, E., Notarnicola, C., Pasolli, L., and Reppucci, A. (2013). Soil  
939 moisture mapping using Sentinel-1 images: Algorithm and preliminary validation. *Remote Sens.*  
940 *Environ.* 134, 234–248.
- 941 Patel, P., and Srivastava, H.S. (2013). Ground truth planning for synthetic aperture radar (SAR):  
942 addressing various challenges using statistical approach. *Int. J. Adv. Remote Sens. GIS Geogr. I*,  
943 1–17.
- 944 Peake, W.H. (1959). Interaction of electromagnetic waves with some natural surfaces. *Antennas*  
945 *Propag. IRE Trans. On* 7, 324–329.
- 946 Prakash, R., Singh, D., and Pathak, N.P. (2012). A fusion approach to retrieve soil moisture with  
947 SAR and optical data. *Sel. Top. Appl. Earth Obs. Remote Sens. IEEE J. Of* 5, 196–206.
- 948 Prévot, L., Champion, I., and Guyot, G. (1993). Estimating surface soil moisture and leaf area  
949 index of a wheat canopy using a dual-frequency (C and X bands) scatterometer. *Remote Sens.*  
950 *Environ.* 46, 331–339.
- 951 Rahman, H., and Dedieu, G. (1994). SMAC: a simplified method for the atmospheric correction  
952 of satellite measurements in the solar spectrum. *Int. J. Remote Sens.* 15, 123–143.
- 953 Saastamoinen, J. (1972). Atmospheric correction for the troposphere and stratosphere in radio  
954 ranging satellites. *Use Artif. Satell. Geod.* 247–251.
- 955 Said, S., Kothyari, U.C., and Arora, M.K. (2012). Vegetation effects on soil moisture estimation  
956 from ERS-2 SAR images. *Hydrol. Sci. J.* 57, 517–534.

- 957 Santi, E., Paloscia, S., Pettinato, S., Notarnicola, C., Pasolli, L., and Pistocchi, A. (2013).  
958 Comparison between SAR soil moisture estimates and hydrological model simulations over the  
959 Scrivia test site. *Remote Sens.* 5, 4961–4976.
- 960 Schwerdt, M., Bräutigam, B., Bachmann, M., and Döring, B. (2008). TerraSAR-X calibration  
961 results. In *Synthetic Aperture Radar (EUSAR), 2008 7th European Conference on*, (Graf-  
962 Zeppelin-Haus, Friedrichshafen, Germany: VDE), pp. 1–4.
- 963 Sikdar, M., and Cumming, I. (2004). A modified empirical model for soil moisture estimation in  
964 vegetated areas using SAR data. In *Geoscience and Remote Sensing Symposium, 2004.*  
965 *IGARSS'04. Proceedings. 2004 IEEE International*, (Anchorage, AK: IEEE), pp. 803–806.
- 966 Simoniello, T., Cuomo, V., Lanfredi, M., Lasaponara, R., and Macchiato, M. (2004). On the  
967 relevance of accurate correction and validation procedures in the analysis of AVHRR-NDVI  
968 time series for long-term monitoring. *J. Geophys. Res. Atmospheres* 1984–2012 109.
- 969 Soon-Koo Kweon, Ji-Hwan Hwang, and Yisok Oh (2012). COSMO SkyMed AO projects -soil  
970 moisture detection for vegetation fields based on a modified water-cloud model using COSMO-  
971 SkyMed SAR data. *Geosci. Remote Sens. Symp. IGARSS Munich Ger. 2012 IEEE Int.* 1204–  
972 1207.
- 973 Srivastava, H.S., Patel, P., Manchanda, M.L., and Adiga, S. (2003). Use of multiincidence angle  
974 RADARSAT-1 SAR data to incorporate the effect of surface roughness in soil moisture  
975 estimation. *IEEE Trans. Geosci. Remote Sens.* 41, 1638–1640.
- 976 Srivastava, H.S., Patel, P., Sharma, Y., and Navalgund, R.R. (2009). Large-area soil moisture  
977 estimation using multi-incidence-angle RADARSAT-1 SAR data. *Geosci. Remote Sens. IEEE*  
978 *Trans. On* 47, 2528–2535.
- 979 Srivastava, H.S., Patel, P., Sharma, K.P., Krishnamurthy, Y.V.N., and Dadhwal, V.K. (2011). A  
980 semi-empirical modelling approach to calculate two-way attenuation in radar backscatter from  
981 soil due to crop cover. *Curr. Sci.* 100, 1871–1874.
- 982 Torre, A., Calabrese, D., and Porfilio, M. (2011). COSMO-SkyMed: Image quality  
983 achievements. In *Recent Advances in Space Technologies (RAST), 2011 5th International*  
984 *Conference on*, (Istanbul, Turkey: IEEE), pp. 861–864.
- 985 Ulaby, F.T., Allen, C.T., Eger Iii, G., and Kanemasu, E. (1984). Relating the microwave  
986 backscattering coefficient to leaf area index. *Remote Sens. Environ.* 14, 113–133.
- 987 Ulaby, F.T., Moore, R.K., and Fung, A.K. (1986). *Microwave Remote Sensing: Active and*  
988 *Passive, vol. III, Volume Scattering and Emission Theory, Advanced Systems and Applications.*  
989 *Inc Dedham Mass. USA Norwood Mass. Artech House* 1797–1848.
- 990 Vermote, E.F., El Saleous, N.Z., and Justice, C.O. (2002). Atmospheric correction of MODIS  
991 data in the visible to middle infrared: first results. *Remote Sens. Environ.* 83, 97–111.

- 992 Wang, S.G., Li, X., Han, X.J., and Jin, R. (2011). Estimation of surface soil moisture and  
993 roughness from multi-angular ASAR imagery in the Watershed Allied Telemetry Experimental  
994 Research (WATER). *Hydrol. Earth Syst. Sci.* *15*, 1415–1426.
- 995 Yang, G., Shi, Y., Zhao, C., and Wang, J. (2012). Estimation of soil moisture from multi-  
996 polarized SAR data over wheat coverage areas. In *Agro-Geoinformatics (Agro-Geoinformatics),*  
997 *2012 First International Conference on*, (Shanghai, China: IEEE), pp. 1–5.
- 998 Yu, F., and Zhao, Y. (2011). A new semi-empirical model for soil moisture content retrieval by  
999 ASAR and TM data in vegetation-covered areas. *Sci. China Earth Sci.* *54*, 1955–1964.
- 1000 Zribi, M., Baghdadi, N., Holah, N., and Fafin, O. (2005). New methodology for soil surface  
1001 moisture estimation and its application to ENVISAT-ASAR multi-incidence data inversion.  
1002 *Remote Sens. Environ.* *96*, 485–496.
- 1003 Zribi, M., Chahbi, A., Shabou, M., Lili-Chabaane, Z., Duchemin, B., Baghdadi, N., Amri, R.,  
1004 and Chehbouni, A. (2011). Soil surface moisture estimation over a semi-arid region using  
1005 ENVISAT ASAR radar data for soil evaporation evaluation. *Hydrol. Earth Syst. Sci.* *15*.
- 1006
- 1007

1008 **List of figures:**

1009 Figure 1. Location of the study site (Domaine du Merle). Black polygons delineate training  
 1010 irrigated grassland plots where ground measurements were made..... 7

1011 Figure 2. Ground-based photographs of study sites illustrating variations in grass growth stages  
 1012 along with in situ measurements..... 14

1013 Figure 3. Sensitivity of radar signal in both HH and HV polarization to volumetric soil moisture.  
 1014 ..... 24

1015 Figure 4. Behavior of WCM components ( $\sigma_{veg}^{\circ}$ ,  $T^2\sigma_{sol}^{\circ}$ , and  $\sigma_{tot}^{\circ}$ ) in both HH and HV  
 1016 polarizations according to  $M_v$ . Black points represent the SAR data ( $\sigma_{tot}^{\circ}$ : real validation dataset)  
 1017 associated with NDVI measurements within  $\pm 0.1$  of the NDVI used in the modelling..... 29

1018 Figure 5. Behavior of WCM components ( $\sigma_{veg}^{\circ}$ ,  $T^2\sigma_{sol}^{\circ}$ , and  $\sigma_{tot}^{\circ}$ ) in both HH and HV  
 1019 polarizations according to NDVI. Black points represent the SAR data ( $\sigma_{tot}^{\circ}$ : real validation  
 1020 dataset) associated with  $M_v$  measurements within  $\pm 5$  vol. % of the  $M_v$  used in the modelling. . 30

1021 Figure 6. Evolution of RMSE of  $M_v$  estimates according to the three inversion configurations as  
 1022 a function of NDVI for noise conditions on the modeled radar signal of  $\pm 0.75$  dB (a), and  $\pm 1$  dB  
 1023 (b)..... 35

1024 Figure 7. Evolution of the relative RMSE (in percent) of  $M_v$  estimates (RRMSE=RMSE/  $M_v$ )  
 1025 according to NDVI and  $M_v$ . (a) configuration 1: HH and NDVI, (b) configuration 2: HV and  
 1026 NDVI, and (c) configuration 3: HH, HV and NDVI. .... 37

1027 Figure 8. Evolution of the bias (estimated  $M_v$  – reference  $M_v$ ) of  $M_v$  estimates according to  
 1028 NDVI values. (a) Inversion configuration 1, (b) inversion configuration 2, and (c) inversion  
 1029 configuration 3..... 38

1030 Figure 9. Evolution of the bias (estimated  $M_v$  – reference  $M_v$ ) on  $M_v$  estimates according to  
 1031 NDVI and  $M_v$  values for noise on the modeled radar signal of 0.75 dB. (a) configuration 1, (b)  
 1032 configuration 2, and (c) configuration 3. .... 40

1033 Figure 10. Box plots of  $M_v$  estimates retrieved from the synthetic dataset. Neural networks were  
 1034 trained and validated according to configuration 3 (using HH, HV and NDVI). Noise on the  
 1035 modeled radar signal is  $\pm 0.75$  dB, and noise on NDVI is 15% of the NDVI value. Values to the  
 1036 right of the box plots represent the RMSE on  $M_v$  estimates for a given reference  $M_v$ ..... 41

1037 Figure 11. Retrieved soil moisture using configuration 1 versus ground-truthed measurements for  
 1038 NDVI lower and higher than 0.75 (a, and b respectively). Noise on radar signal =  $\pm 1$ dB. Bias =  
 1039 estimated  $M_v$  - reference  $M_v$ ..... 49

1040